UNIVERSITÁ DEGLI STUDI DI NAPOLI FEDERICO II

Scuola Politecnica e delle Scienze di Base

Laurea Magistrale in Ingegneria Elettronica

Beam equipment electromagnetic interaction in accelerators: simulation and experimental benchmarking

University Advisors:
Prof Rita Massa
Prof. Vittorio Giorgio Vaccaro
Prof. MariaR. Masullo

Candidate:
Andrea Passarelli
Matr. M61/082

CERN Advisor:
Dott. Ing. Carlo Zannini

Anno Accademico 2013/2014

Contents

Contents **i**

Acknowledgements **iii**

Introduction **1**

1 CERN **4**
- 1.1 What is CERN . . . 4
- 1.2 The accelerator chain . . . 4
- 1.3 The Large Hadron Collider . . . 5
  - 1.3.1 The purpose . . . 6
  - 1.3.2 The LHC project . . . 6
  - 1.3.3 The LHC detectors . . . 9
  - 1.3.4 Future upgrades . . . 10

2 Wakefields and Impedance **11**
- 2.1 Longitudinal Wake function and coupling impedance . . . 12
  - 2.1.1 Energy loss . . . 13
- 2.2 Transverse Wake function and coupling impedance . . . 15

3 CST Studio Suite **18**
- 3.1 Wakefield solver . . . 18
- 3.2 Eigenmode solver . . . 20

4 EM simulations of the UA9 goniometer and experimental benchmarks **22**
- 4.1 Introduction . . . 23
- 4.2 Simplified models . . . 24
  - 4.2.1 Pillbox cavity with and without crystal . . . 24
  - 4.2.2 Pillbox cavity with crystal and holder . . . 31
  - 4.2.3 Pillbox cavity with holes . . . 33
- 4.3 CST detailed geometry and comparison with wire measurements . . . 37

5 Beam coupling impedance measurements below the pipe cut-off frequency: numerical investigations **39**
- 5.1 Introduction . . . 39
- 5.2 Example of application: a pillbox cavity . . . 41

5.2.1 Analytical model of resonant frequencies and quality factors 42
5.2.2 Analytical calculation of the beam coupling impedance by using the mode matching technique 47
5.2.3 Comparison among CST simulations, analytical formula and Mode Matching results 49
5.2.4 Measurements with probes 51
5.2.4.1 Measurements of resonant frequencies and quality factors 52
5.3 An hybrid numerical/experimental method to compute the beam coupling impedance 53
5.3.1 Comparison between the hybrid method and the mode matching technique 54

Conclusion **56**

A Symmetries **59**

Bibliography **64**

Ad Antonio, Attilio,
Gisella, Maria,
Peppa e Peppino.

Acknowledgements

This thesis is the result of a whole year of work, spent at the *Conseil Européen pour la Recherche Nucléaire (CERN)* as a technical student. I really enjoyed this experience mostly because of the people I met. Every one of them taught me something very valuable that increased my experience baggage.

I am heartily grateful to Prof. Vaccaro, my University supervisor, for giving to me the possibility of working in a stimulating environment, where I confronted myself with the real scientific world and I put what I have studied in books in practice.

A special thank goes to Carlo Zannini, my CERN supervisor, who patiently helped me during all the steps of this thesis writing with a lot of precious suggestions and for the time spent talking about Naples soccer club tactics.

I cannot forget to thank Alessandro Danisi for his helpful support on UA9 experiment and also for his friendly Neapolitan humor.

A great thank goes to Prof. Masullo and Prof. Massa for their constant willingness to help me any time and for gentle manner they always have.

I am very grateful to Elias Métral, Benoit Salvant and Giovanni Rumolo, my leaders during my technical student period, who always supported my initiatives.

I am also very grateful to the other people I worked with, they helped me during my researches in various ways. The friendly working environment established by them was one of the reasons why waking up early in the morning was not so bad.

See you the next goal!

Introduction

In particle accelerators, the electromagnetic interaction between beam particles and their surroundings have attracted the attention of physicists and engineers since the beginning of the systematic study of coherent instabilities[1][2][3][4][5]. The strength of the interaction is characterized by the definition of beam coupling impedance (and wake field) of the accelerator components. The beam coupling impedance plays a key role in the behaviour of any circular accelerator, because limiting its performances and need to be taken carefully into account in the design of new machines. In order to understand the concept of the impedance we refer to the loop diagram in Fig.1. As one may understand, the beam current J and the electromagnetic field play two different roles. At the same time they are:

- the forcing term of Maxwell's equations and beam dynamics equations, respectively,
- the solution of the beam dynamics equations and Maxwell's equations respectively.

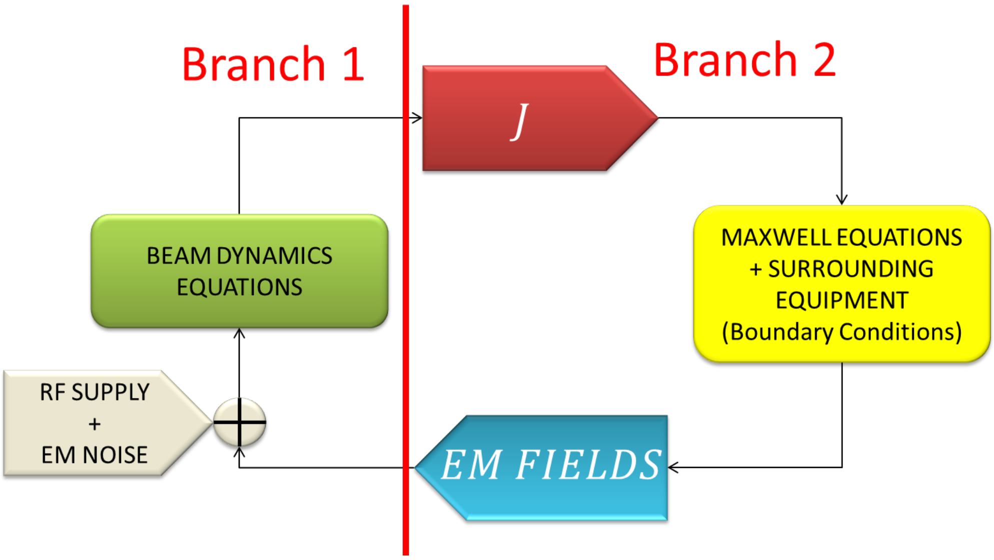

Figure 1: The stability problem: the flow chart of the coupled equations.

Let us start from the beam current J, in the red frame, this can be considered as the driving term of Maxwell's equations which must be solved taking into account the boundary conditions. Solving this problem we get the electromagnetic fields $\overrightarrow{E}$ and $\overrightarrow{H}$ in the beam pipe. These fields (together with noise and RF supply) act as input of the beam dynamics equations. The solution of these equations give as output the beam current J. The beam in a circular accelerator behaves as a feedback circuit which may exhibit unstable solutions.

As consequence of the described loop behaviour, a small perturbation on a theoretically stable beam distribution may induce another perturbation enhancing the previous one.

The study and the solution of branch # 2 lead to a transfer function between a possible perturbation and the electromagnetic fields, produced in the interaction with the beam pipe.

In the frequency domain this problem can be described trough a transfer function is defined as the coupling impedance; in the time domain as the wake fields.

According to the type of perturbation (longitudinal or transverse), we define a longitudinal or transverse impedance $(Z_{\|}, Z_{\perp})$ in the frequency domain. Similarly we define longitudinal and transverse wake fields.

The study of the branch # 1 leads to a stability criterion which relates the high energy experiment requirements to the parameter Z[1][2][3][4][5].

In particular, for longitudinal motion in the frequency domain the beam will be stable if the following inequality is satisfied:

$$|Z_{\|}| < K \frac{(\Delta E)^2}{I_0} \tag{1}$$

where ΔE is the energy spread in the beam, the I_0 is the mean beam current and K is a known constant which depends on the characteristic parameter of the accelerator.

One may understand that this criterion is conflicting with the required beam characteristics for more and more demanding experiments. In general, experimental physicist require very small spread ΔE in energy and very high current I_0 intensity; this implies that the "impedance budget" is very small. On the other hand this impedance will be the sum of all the contributions due to all the items inserted in the accelerator vacuum chamber, which may electromagnetically interact with the beam. These items are becoming more and more copious. Therefore, the efforts of the designer are devoted to the reduction of the coupling impedance in order to stay in the limit of this budget.

The computation of this budget makes use of theoretical analysis, computer simulations, and experimental measurements before the installation of the critical items.

This thesis developed within two groups of researches, one at CERN of Geneva and the other of Istituto Nazionale di Fisica Nucleare (INFN) of Naples, is devoted to the study

of the impedance of the LHC goniometer, used for beam collimation.
Two aspects will be dealt with:

- the simulation analysis to understand the influence of each part of the complex goniometer geometry on the global behaviour of the impedance (see Ch.4),
- the study and development of a new experimental/numerical method to evaluate the beam impedance below the cut-off frequency of the pipes(see Ch.5).

This thesis has been subdivided into 5 Chapters and can be summarized as follows:

- in the **Chapter 1** the CERN and the LHC experiment are introduced;
- in the **Chapter 2** the key concepts of wake function and beam coupling impedance are explained;
- in the **Chapter 3** a description of the electromagnetic CAD is reported. In particular the wakefield solver and the eigenmode solver;
- the **Chapter 4** describes step by step the simulation performed to evaluate the LHC goniometer beam coupling impedance resorting to electromagnetic codes. The codes have shown resonant modes in the frequency band of our interest. This study has clearly shown that numerical modelling is problematic for structures with non-elementary geometries or composed by materials with unknown or complex electromagnetic properties (e.g. the material roughness);
- the **Chapter 5** deal with a benchmark on a numerical/experimental method performed to evaluate the beam coupling impedance even for non-elementary structures. For the validation of this method a pillbox cavity has been characterized comparing analytical formulas, numerical results and experimental measurements.

Chapter 1

CERN

1.1 What is CERN

Founded in 1954, the CERN laboratory is located at the French-Swiss border, between the Jura mountains and Geneva's lake. The acronym CERN stands for European Organization for Nuclear Research, institution founded in 1954, with the mandate of establishing a world-class fundamental physics research organization in Europe. CERN provides to scientists with particle accelerators, detectors, and infrastructure in order to set up experiments needed to go deeper in our understanding of matter, particle physics and Universe. Currently, the CERN laboratory counts 20 Member States, 8 "Observers", and provides facilities to 580 institutes and universities involving 85 nationalities .

1.2 The accelerator chain

In Fig1.1 we can have a look of the accelerators chain at CERN. A brief description of the LHC beam route follows.

LINAC2: Hydrogen atoms are taken from a standard hydrogen bottle, then protons are obtained by stripping electrons o atoms. Protons produced with a kinetic energy of 100 keV are injected in a RF Quadrupole where they are focused and accelerated at the same time. When they reach 750 keV they are injected in LINAC2, a linear accelerator, where they get 50 MeV energy at extraction.

PSB: Protons are injected in the PSB (Proton Synchrotron Booster), a particular accelerator built in 1972 with four rings superimposed. Here the beam reaches 1.4 GeV top energy.

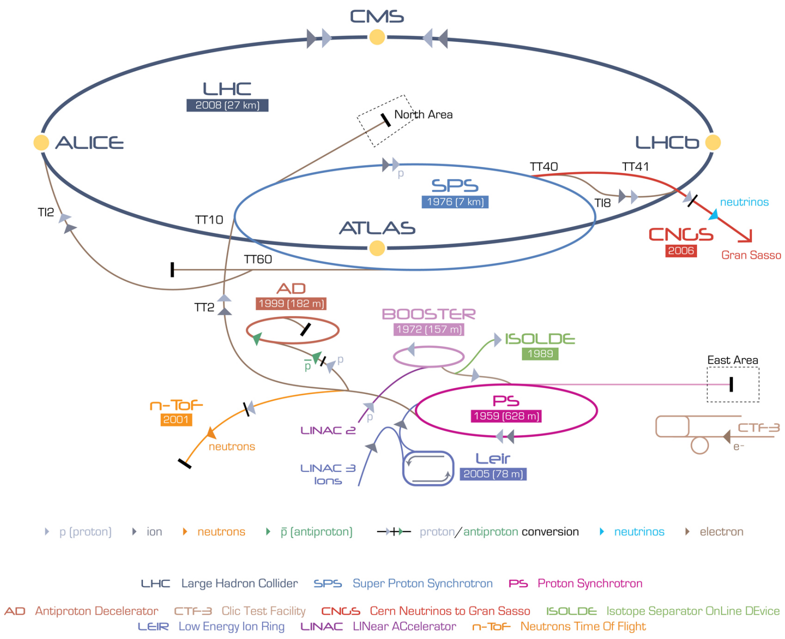

FIGURE 1.1: CERN accelerator complex.

PS: Built in 1972, the Proton Synchrotron is the oldest machine at CERN and, in its long working experience, managed many different kind of particles: protons, antiprotons, electrons, positrons and various species of ions. It injects the beam in SPS at 25 GeV via TT2 and TT10 transfer lines.

SPS: The Super Proton Synchrotron is a circular proton accelerator with a circumference near $7Km$. SPS was used also as a proton - antiproton collider, making possible in 1983 the W and Z bosons discovery. Here the beam is accelerated up to 450 GeV/c, ready to be injected in LHC via TT60/TI2 and TT40/TI8 transfer lines.

LHC: The beam coming from SPS is injected in the 27 Km long Large Hadron Collider. The clockwise and anticlockwise bunches can reach at the moment 4 TeV energy under normal operating conditions and collide in one of the four Interaction Points (IPs) where huge detectors are positioned. At nominal working conditions, the machine will host 2808 $25ns$-spaced, $1.12ns$-long bunches, each one with an intensity of $1.15 \cdot 10^{11}$ protons per bunch, in order to reach a peak luminosity of $10^{34}cm^{-2}s^{-1}$.

1.3 The Large Hadron Collider

The Large Hadron Collider (LHC) is an example of circular particle accelerator for high energy physics experiment. It has been built by the European Organization for Nuclear Research (CERN) near Geneva. The LHC has been completed on July 2008 and tested for the first time on September, 10, 2008 with its first circulating beam.

Figure 1.2: Overview of the Geneva area with superposed the track of LHC.

1.3.1 The purpose

The Higgs boson, the last particle among those predicted by the Standard Model has been observed. The verification of the existence of the Higgs boson also explain the mechanism of electroweak symmetry breaking, through which the particles of the Standard Model are thought to acquire their mass. In addition to the Higgs boson, new particles predicted by possible extensions of the Standard Model might be produced at the LHC. The LHC physics program is mainly based on proton-proton collision. However, shorter running periods, typically one month per year, with heavy-ion collisions are included in the program. While lighter ions are considered as well, the baseline scheme deals with lead ions. This will allow an advancement in the experimental program currently in progress at the Relativistic Heavy Ion Collider (RHIC). The aim of the heavy-ion program is to provide a window on a state of matter known as Quark-gluon plasma, which characterized the early stage of the life of the Universe.

1.3.2 The LHC project

The LHC is the world's largest and highest-energy particle accelerator. The collider is contained in a circular tunnel, with a circumference of 27 kilometres, at a depth ranging from 50 to 175 meters underground.

The 3.8 m wide concrete-lined tunnel, constructed between 1983 and 1988, was Large Electron-Positron Collider (LEP). It crosses the border between Switzerland and France at four points, with most of it in France. Surface buildings hold ancillary equipment such as compressors, ventilation equipment, control electronics and refrigeration plants[6].

The collider tunnel contains two adjacent parallel beam pipes that intersect at four

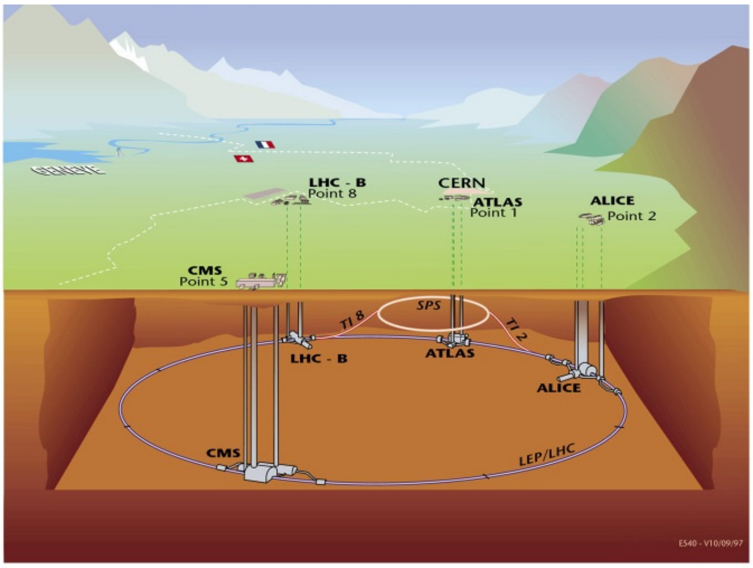

FIGURE 1.3: Overall view of the LHC experiments.

points, each containing a proton beam, which travel in opposite directions around the ring.

Different magnets are used to ”contain” the beam inside the accelerator. 1232 dipole magnets keep the beams on their circular path, while an additional 392 quadrupole magnets are used to keep the beams focused, in order to maximize the chances of interaction between the particles in the four intersection points, where the two beams will cross. In total, over 1600 superconducting magnets are installed, with most weighing over 27 tonnes. The technical data regarding the dipole magnets are summarized in table 1.

Approximately 96 tons of liquid helium are needed to keep the magnets at their operating temperature, making the LHC the largest cryogenic facility in the world at liquid helium temperature. Superconducting quadrupole electromagnets are used to direct the beams to four intersection points, where interactions between protons will take place. Once or twice a day, as the protons are accelerated from 450 GeV to 7 TeV, the field of the superconducting dipole magnets will be increased from 0.54 to 8.3 Tesla (T).

In the final configuration protons will have an energy of 7 TeV, giving a total collision energy of 14 TeV. At this energy the protons have a Lorentz factor of about 7500 and move at about 99.9999991% of the speed of light. It will take less than 90 μs for a proton to travel once around the main ring (a frequency of about 11000revolutions per second). Rather than continuous beams, the protons will be bunched together, into 2808 bunches, so that interactions between the two beams will take place at discrete intervals never shorter than 25 ns.

Prior to being injected into the main accelerator, the particles are prepared by a series of system that successively increase their energy, as depicted in Fig.1.4. The first system is the linear particle accelerator LINAC 2 generating 50 MeV protons, which feeds the

Magnetic Length	14.3 m
Operating Temperature	1.9 K
Current at injection (0.45 TeV)	739 A
Bending radius	2803.928 m
Number of beams per magnet	2
Nominal current	1850 A
Bending angle per magnet	5.1000 $mrad$
Peak field in coil	8.76 T
Field at injection	0.535 T
Field at 74 TeV	8.33 T
Inductance per magnet	0.108 H
Mass of cold mass	23.8 t

Table 1.1: Dipole magnets general data.

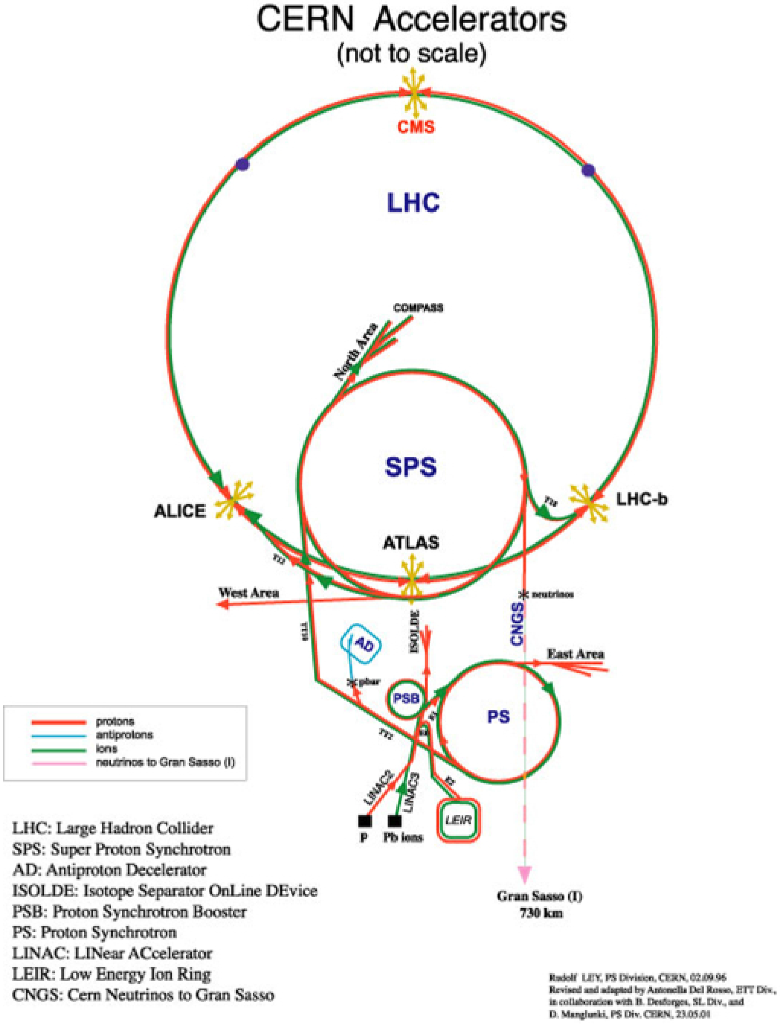

Figure 1.4: Acceleration system for the LHC preliminary acceleration.

Proton Synchrotron Booster (PSB). There the protons are accelerated to 1.4 GeV and injected into the Proton Synchrotron (PS), where they are accelerated to 26 GeV. Finally the Super Proton Synchrotron (SPS) is used to further increase their energy to 450

GeV before they are at last injected (over a period of 20 minutes) into the main ring. Here the proton bunches are accumulated, accelerated (over a period of 20 minutes) to their peak 7 TeV energy, and finally circulated for 10 to 24 hours while collisions occur at the four intersection points. The general technical data are summarized in Tab.1.2. The LHC will also be used to collide lead (Pb) heavy ions. The Pb ions will be first accelerated in the linear accelerator LINAC 3, and Low-Energy Injector Ring (LEIR) will be used as an ion storage and cooler unit. The ions then will be further accelerated by the PS and SPS before being injected into LHC ring, where they will reach an energy of 2.76 TeV per nucleon.

Maximum kinetic of a proton	7 TeV
Strength of dipole magnets	8.33 T
Number of particles per bunch	1.1×10^{11}
Circulating current per beam	0.54 A
RMS bunch length	7.5 cm
Bunch spacing	25 ns
Tunnel circumference	27 km
Number of bunches around ring	2808
Number of dipole magnet	1232
Length of each dipole magnet	4.3 m
Maximum proton velocity	$0.99999991c$
Injection Energy	450 GeV
Energy loss per turn	6.7 keV

Table 1.2: General technical data for the Large Hadron Collider.

1.3.3 The LHC detectors

Six detectors have been constructed at the LHC, located underground in large caverns excavated at the LHC's intersection points. Two of them, the ATLAS experiment and the Compact Muon Solenoid (CMS), are large, general purpose particle detectors. A Large Ion Collider Experiment (ALICE) and LHCb have more specific roles and the last two TOTEM and LHCf are very much smaller and are for very specialized research. ATLAS is one of two so-called general purpose detectors. ATLAS will be used to look for signs of new physics, including the origins of mass and extra dimensions. CMS is the other general purpose detector by which the Higgs boson has been discovered and looks for the origin of the nature of the dark matter. ALICE will study a "liquid" form of matter called quark-gluon plasma that existed shortly after the Big Bang. Equal amounts of matter and anti-matter were created in the Big Bang. LHCb will try to investigate what happened to the "missing" anti-matter.

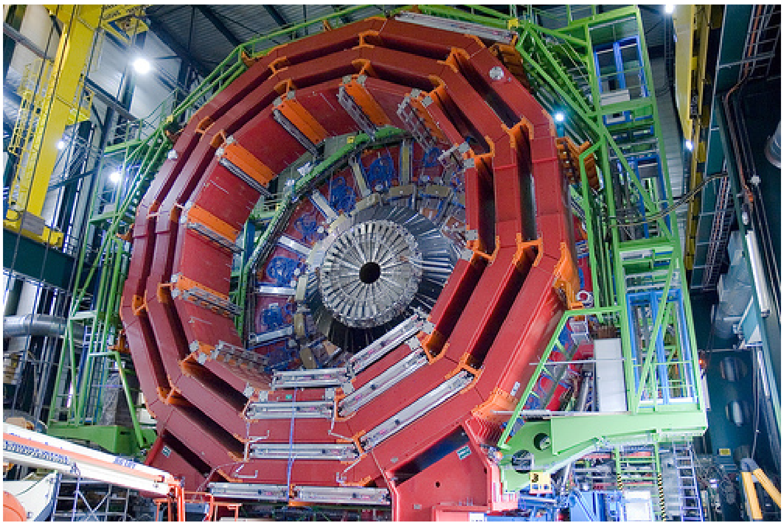

Figure 1.5: The CERN Compact Muon Solenoid detector (CMS).

1.3.4 Future upgrades

After some years of running, any particle physics experiment typically begins to suffer from diminishing returns; each additional year of operation discovers less than the year before. The way around the diminishing returns is to upgrade the experiment, either in energy or in luminosity. A luminosity upgrade of the LHC, called the Super LHC, has been proposed, to be made after ten years of LHC operation. The optimal path for the LHC luminosity upgrade includes an increase in the beam current (i.e., the number of protons in the beams) and the modification of the two high-luminosity interaction regions, ATLAS and CMS. To achieve these increases, the energy of the beams at the point that they are injected into the (Super) LHC should also be increased to 1 TeV. This will require an upgrade of the full pre-injector system, the needed changes in the Super Proton Synchrotron being the most expensive.

The size of the LHC constitutes an exceptional engineering challenge with unique operational issues on account of the huge energy stored in the magnets and the beams. While operating, the total energy stored in the magnets is 10 GJ (equivalent to one and a half barrels of oil or 2.4 tons of TNT) and the total energy carried by the two beam reaches 724 MJ (about a tenth of a barrel of oil, or half a lightning bolt).

Loss of only one ten-millionth part (10^{-7}) of the beam is sufficient to quench a superconducting magnet, while the beam dump must absorb 362 MJ, an energy equivalent to that of burning eight kilograms of oil, for each of the two beams. These immense energies are even more impressive considering how little matter is carrying it: under nominal operating conditions ($2,808$ bunches per beam, 1.1×10^{11} protons per bunch), the beam pipes contain 1.0×10^{-9} gram of hydrogen, which, in standard conditions for temperature and pressure, would fill the volume of one grain of fine sand.

Chapter 2

Wakefields and Impedance

In this chapter, we first introduce the concept of wake function and beam coupling impedance treating separately the longitudinal and transverse planes. In the longitudinal plane we also discuss the relationship between the beam coupling impedance and the energy loss by a bunch of charged particles.

The wake functions describe the interaction of the beam with the surrounding environment. The electromagnetic (EM) problem is posed setting the Maxwell's equations with the beam as source term and boundary conditions given by the structure in which the beam propagates. Wake fields (time domain) and Impedances (frequency domain) allow describing in a sufficiently general way the effects of the self-induced fields on the beam. A particle q_0 going through a device of length $L, s(0, L)$, leaves behind an oscillating field, probe charge q at distance z will feel a force as a result (Fig.2.1)[7].

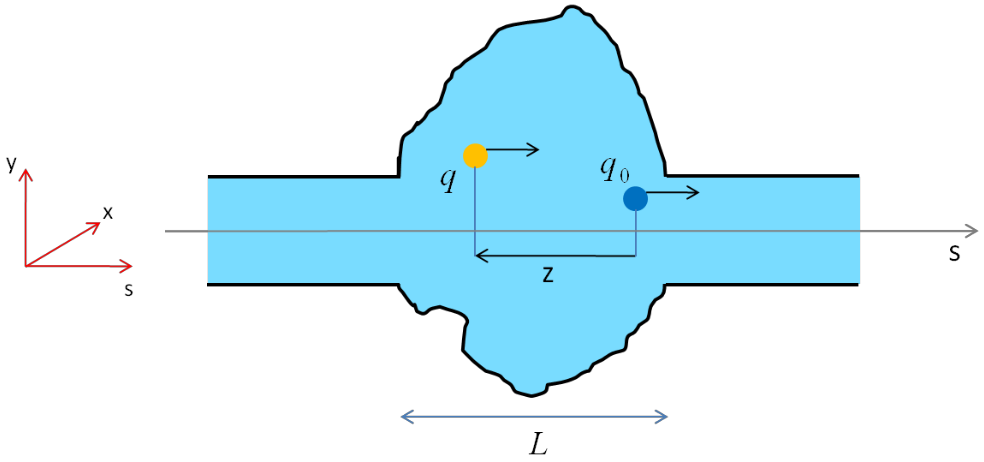

FIGURE 2.1: Device of arbitrary cross section along an accelerator.

The integral of this force over the device length defines the wake function and its Fourier transform is called the impedance of the device of length L. The particles are assumed to move with the same velocity $v = \beta c$, where c is the speed of light and β is the relativistic factor.

2.1 Longitudinal Wake function and coupling impedance

The longitudinal wake function of an accelerator component is basically its Green function in the time domain [8] (i.e., its response to a pulse excitation) and is defined as follow:

$$W_{||}(x, y, x_0, y_0, z)[V/C] = -\frac{1}{q_0 q} \int_0^L F_{||}(x, y, s, x_0, y_0, z) ds \tag{2.1}$$

where $F_{||}(x, y, s, x_0, y_0, z) = q e_s(x, y, s, x_0, y_0, z)$ is the longitudinal component of Lorentz's force, $e_s(x, y, s, x_0, y_0, z)$ is the longitudinal component of the electric field $\vec{e}(x, y, s, x_0, y_0, z))$ induced by the source charge q_0; (x_0, y_0) and (x, y) define respectively the transverse offset of source and test particle with respect to the geometric center of the structure. The wake function of Eq. 2.1 can be expanded into a power series in the offset of source and test particle. The classical longitudinal wake function is defined as the zeroth order term of this series. This definition leads to a longitudinal wake function independent of the offsets of both source and test particle. In axisymmetric structures (or simply with left/right and top/bottom symmetry), if both source and test particle are in the center of symmetry of the accelerator element: $(x_0, y_0) = (0, 0)$ and $(x, y) = (0, 0)$, the longitudinal wake function reduces exactly to the zeroth order term. The definition of wake function is very useful for macroparticle models and simulations, because it can be used to describe the driving terms in the single particle equations of motion. We can also describe it as a transfer function in the frequency domain [2],[9]. The longitudinal beam coupling impedance of the element under study is than defined as follows:

$$Z_{||}[\Omega] = \int_{-\infty}^{\infty} W_{||}(z) e^{-\frac{j\omega z}{v}} \frac{dz}{v} \tag{2.2}$$

Here j is the imaginary unit and $\omega = 2\pi f$ is the angular frequency conjugate variable of the time delay $\tau = \frac{z}{v}$. The impedance can be defined also directly in frequency domain as follows [10]:

$$Z_{||}(x, y, x_0, y_0, \omega)[\Omega] = -\frac{1}{q_0} \int_0^L E_s(x, y, s, x_0, y_0, \omega) e^{jks} ds \tag{2.3}$$

where $E_s(x, y, s, x_0, y_0, \omega)$ is the longitudinal component of the electric field in frequency domain and $k = \frac{\omega}{v}$ is the wave number. In the following, EM fields in frequency domain will be indicated with capital letter to be distinguished from the fields in time domain, indicated by the respective low-case letters. The value of the wake function in 0, $W_{\|}(0)$, is related to the energy lost by the source particle in the creation of the wake:

$$W_{\|}(0) = -\frac{\Delta E_1}{q^2} \tag{2.4}$$

$W_{\|}(0) > 0$ since $\Delta E_1 < 0$. $W_{\|}(z)$ is discontinuous in $z = 0$ and it vanishes for all $z < 0$ in case of ultra-relativistic approximation ($\beta = 1$). In the global energy balance, the energy lost by the source splits into: electromagnetic energy of modes that propagate down the beam chamber (above cut-off), which will be eventually lost on surrounding lossy materials, and electromagnetic energy of the modes that remain trapped in the device. In the second case two scenarios are possible: 1) this energy can be dissipated on lossy walls or trough purposely designed HOM absorbers; 2) it keeps ringing without damping (perfect electric conducting (PEC) walls), but can also be transferred to following particles (or the same over several turns) passing trough the device, possibly feeding into an instability.

2.1.1 Energy loss

Let us consider a bunch of particles with line density $\lambda(z)$ (normalized to unity) passing once through an accelerator device generating a wake function$W_{\|}(z)$. The energy kick $\Delta E(z)$ on the witness slice $eN_{bunch}\lambda(z)dz$ (e is charge of the particle and N_{bunch} is the number of particles in the bunch) is the integral of the contributions from the wakes left behind by all the preceding $eN_{bunch}(z')dz$ slices (sources) (Fig.2.2).

The total energy loss ΔE of the bunch can then be obtained by integrating $\Delta E(z)$ over the full bunch extension:

$$\Delta E = \int_{-\hat{z}}^{\hat{z}} \lambda(z)\Delta E(z)dz \tag{2.5}$$

with:

$$\Delta E(z) = e^2 N_{bunch}^2 \int_{-\hat{z}}^{\hat{z}} \lambda(z')W_{\|}(z - z')dz' \tag{2.6}$$

Transforming Eq.2.5 into the frequency domain yields:

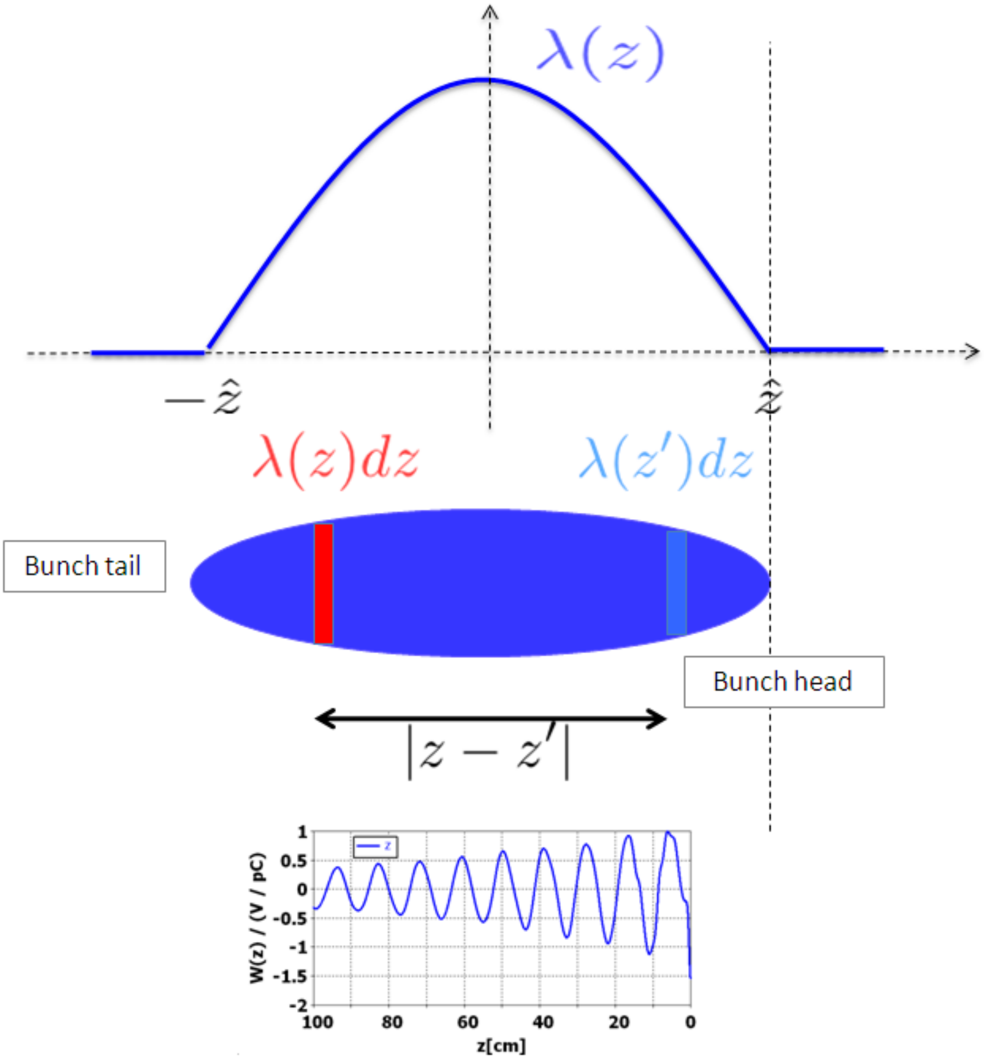

FIGURE 2.2: Bunch spatial distribution (at the top). The bunch is divided in slices (in the center). Each slice leaves behind a wake-field (at the bottom).

$$\Delta E = \frac{e^2 N_{bunch}^2}{2\pi} \int_{-\infty}^{\infty} |\bar{\lambda}(\omega)|^2 Re[Z_{\parallel}(\omega)] d\omega \tag{2.7}$$

Considering a bunch of particles that passes many times through the accelerator structure the total energy loss ΔE of the bunch can still be obtained by integrating $\Delta E(z)$ over the full bunch extension. $\Delta E(z)$ this time also includes the contributions from all previous turns, spaced by multiples of the ring circumference C:

$$\Delta E = \frac{e^2 N_{bunch}^2}{2\pi} \int_{-\infty}^{\infty} \lambda(z) dz \int_{-\infty}^{\infty} \lambda(z') \sum_{k=-\infty}^{+\infty} W_{\parallel}(kC + z - z') dz' \tag{2.8}$$

Considering the following relationship:

$$\sum_{k=-\infty}^{+\infty} W_{\|}(kC + z - z') = \frac{c}{C} \sum_{p=-\infty}^{+\infty} Z_{\|}(p\omega_0) e^{-\dfrac{jp\omega_0(z-z')}{c}} \tag{2.9}$$

we obtain:

$$\Delta E = \frac{e^2 N_{bunch}^2 \omega_0}{2\pi} \sum_{p=-\infty}^{+\infty} |\bar{\lambda}(p\omega_0)|^2 Re[Z_{\|}(p\omega_0)] \tag{2.10}$$

where $\bar{\lambda}(p\omega_0)$ is the Fourier transform of $\lambda(z)$ evaluated in $p\omega_0$. The formula can be easily extended to the case of a beam of any number of bunches $n_{bunches}$, that passes many times through the structure, by replacing the bunch spectrum $\bar{\lambda}(p\omega_0)$ with the beam spectrum $\bar{\Lambda}(p\omega_0)$ and the intensity of the bunch N_{bunch} with the intensity of the beam $N_{beam} = n_{bunches}N_{bunch}$ (total number of particles in the beam). The power loss on the device $\Delta E f_0$, where f_0 is the revolution frequency of particles in the ring of circumference C, is an important quantity since it directly relates to the beam induced heating.

2.2 Transverse Wake function and coupling impedance

In an axisymmetric structure, or simply one with only a top-bottom or left-right symmetry, a source particle travelling on axis cannot induce net transverse forces on a witness particle also following on axis. We need to introduce a breaking of the symmetry to drive transverse effect, i.e. offset the source or the witness. The transverse wake functions are defined as:

$$W_{x,y}(x, y, x_0, y_0, z)[V/C] = -\frac{1}{q_0 q} \int_0^L F_{x,y}(x, y, s, x_0, y_0, z) ds \tag{2.11}$$

where $F_{x,y}(s, z) = [q(\vec{e}(x, y, s, x_0, y_0, z) + \vec{v} \times \vec{b}(x, y, s, x_0, y_0, z))]_{x,y}$ are the transverse components of Lorentz's force; $\vec{b}(x, y, s, x_0, y_0, z)$ is the magnetic induction field. Similarly to its longitudinal counterpart the transverse wake functions of Eq.2.11 can be expanded into a power series in the offset of source and test particle. Since no transverse effects can appear when both source and test particle are in the center of symmetry, the zeroth order term of the power series is null. Considering only the first order terms and disregarding possible coupling between transverse planes we can write:

$$\begin{aligned} W_x &= W_x^{driv} x_0 + W_x^{det} x \\ W_y &= W_y^{driv} y_0 + W_y^{det} y \end{aligned} \tag{2.12}$$

where $W_{x,y}^{driv}$ is the horizontal/vertical driving (also called dipolar) wake function and $W_{x,y}^{det}$ is the horizontal/vertical detuning (also called quadrupolar) wake function. For small offsets of both source and test particle, Eq.2.12 is a very good approximation of the transverse wakes. From Eq.2.12 we find the following relationship to disentangle driving and detuning contributions:

$$\begin{aligned} W_x^{driv}(z)\left[\frac{V}{mC}\right] &= \left.\frac{W_x(z)}{x_0}\right|_{x=0} \\ W_x^{det}(z)\left[\frac{V}{mC}\right] &= \left.\frac{W_x(z)}{x}\right|_{x=0} \\ W_y^{driv}(z)\left[\frac{V}{mC}\right] &= \left.\frac{W_y(z)}{y_0}\right|_{y=0} \\ W_y^{det}(z)\left[\frac{V}{mC}\right] &= \left.\frac{W_y(z)}{y}\right|_{y=0} \end{aligned} \tag{2.13}$$

The sum of driving and detuning contributions define the generalized term $W_{x,y}^{gen}$. As for the longitudinal case, the transverse wake function of an accelerator component can be viewed as basically its Green function in the time domain (i.e., its response to a pulse excitation). It is very useful for macroparticle models and simulations, because it relates source perturbations to the associated kicks on trailing particles:

$$\begin{aligned} \Delta x' \ \alpha \ W_x(z) &= W_x^{driv}(z) x_0 + W_x^{det}(z) x \\ \Delta y' \ \alpha \ W_y(z) &= W_y^{driv}(z) y_0 + W_y^{det}(z) y \end{aligned} \tag{2.14}$$

Moreover, from Maxwell's equations and the definitions of wake functions one can derive the general relation [11]:

$$\frac{\partial W_x(z)}{\partial x} = -\frac{\partial W_y(z)}{\partial y} \tag{2.15}$$

from which it follows that:

$$W_x^{det}(z) = -W_y^{det}(z) \tag{2.16}$$

Likewise to the longitudinal case the transverse beam coupling impedance of the element under study is defined as the Fourier transform of the respective wake function:

$$\begin{aligned} Z_\perp^{driv}(\omega)[\Omega/m] &= j\int_{-\infty}^{\infty} W_\perp^{driv}(z)e^{-\frac{j\omega z}{v}}\frac{dz}{v} \\ Z_\perp^{det}(\omega)[\Omega/m] &= j\int_{-\infty}^{\infty} W_\perp^{det}(z)e^{-\frac{j\omega z}{v}}\frac{dz}{v} \end{aligned} \tag{2.17}$$

Furthermore, as for the longitudinal case we can define the transverse impedance directly in the frequency domain:

$$\begin{aligned} Z_x(x,y,x_0,y_0,\omega)[\Omega] &= \frac{j}{q_0}\int_0^L [E_x - \beta Z_0 H_y](x,y,x_0,y_0,\omega)e^{jks}ds \\ Z_y(x,y,x_0,y_0,\omega)[\Omega] &= \frac{j}{q_0}\int_0^L [E_y + \beta Z_0 H_y](x,y,x_0,y_0,\omega)e^{jks}ds \end{aligned} \tag{2.18}$$

where Z_0 is the free space impedance ($120\pi\Omega$). Analogously to its equivalent in the time domain the impedance of Eq.2.18 can be expanded into a power series in the offsets of source and test particle:

$$\begin{aligned} Z_x &= Z_x^{driv}x_0 + Z_x^{det}x \\ Z_y &= Z_y^{driv}y_0 + Z_y^{det}y \end{aligned} \tag{2.19}$$

The 2.19 are the horizontal and vertical component of the beam coupling impedance and their dimension is $\left[\frac{\Omega}{m}\right]$.

It is important to underline that the longitudinal and transverse wakes, defined in the chapter, are the response to a pulse excitation seen as a single particle: they are identified as wake function.

If the source is a bunch of particles the resulting wake will be given by the convolution of the wake function by the charge density of the bunch $\lambda(z)$ and is called wake potential. Applying the convolution theorem, the beam coupling impedance as defined in Eq.2.1 can be calculated as the Fourier transform of the wake potential divided by the Fourier transform of the line density. This point has to taken into account in the evaluation with the electromagnetic cad.

Chapter 3

CST Studio Suite

The software used in this work, CST Studio Suite, is a commercial 3-D electromagnetic Computer Aided Design (CAD) software. In particular this thesis will focus on the use of time domain 3D CST Particle Studio EM simulations to calculate wake and impedance values and frequency domain 3D CST Microwave studio EM simulations to evaluate the resonant frequencies and merit factors in the resonant cavities.

3.1 Wakefield solver

The Wakefield solver of Particle Studio (PS) solves Maxwell's equations in time domain (TD), using a particle bunch as excitation of the structure under study. Standard outputs of the code are the wake potentials produced by the exciting Gaussian bunch (called 'source') as a function of the time delay τ with respect to the passage of the source (i.e. the integrated electromagnetic force felt by a witness charge that goes through the structure a time τ behind the source) and its equivalent in frequency domain (FD), the Fourier transform normalized to the bunch spectrum, the beam coupling impedance. Besides, since the code allows defining separately the transverse position of the exciting bunch and that of the computation point, we can also separately simulate the driving and the detuning terms of the transverse wake potentials[7].

Wakefield solver: settings
To set up the calculations efficiently in terms of accuracy of the results and of computing time, a wise choice of some numerical and physical parameters of the solver becomes crucial. Here follows a list of the most relevant ones:

LW: the reliability of the EM simulation is related to the accuracy of the discretization of the computational domain. Concerning this aspect the main parameter for the user is the number of mesh lines per wavelength (LW). The stability of the results for the device under test (DUT) must be checked with respect to this parameter to set up its value according to the demanded accuracy of the results. The time of the calculation significantly increases with the density of the mesh since the time step is directly related to the minimum mesh step width used in the discretization of the structure.

σ_z: the standard deviation of the source Gaussian bunch (RMS bunch-length) is crucial both for TD (Wake-field) and FD (Impedance) results. Since we are interested in the wake functions, because of beam dynamics studies, we would like to have a bunch length σ_z comparable with the thickness of the slices needed for the beam dynamics calculation. Decreasing σ_z , also the wavelength decreases by the same factor. This allows for a larger range of frequencies to be explored but also requires a proportional increase of mesh cells to keep the lines of mesh per wavelength constant. The choice of a value for σ_z turns out to be a trade-off between the special needs of the simulation. Concerning impedance studies the choice of σ_z is determined by the range of frequency that we are interested to analyze.

WL: the simulated wake length limits the calculation of the wakes to a distance WL from the source and plays an important role on the accuracy of the impedance results.

Source offsets: for the simulation of transverse wakes (driving and detuning) it is important to use an offset from the source small enough to stay in the region where the linear approximation of the wake functions made in Eq.2.12 remains valid. Otherwise, it is important to mention that the use of a very small displacement for the calculation of the transverse impedance can lead to numerical issues.

Integration method: the wake potentials by default are calculated by integrating the electromagnetic force along the z-axis (direct integration scheme). Indirect integration schemes are also available: the indirect test-beam and interfaces. These methods can be more accurate, but require some extra conditions. The indirect test-beam method computes the wake potential by recording the longitudinal field values on the extruded shell of the beam tube in the discontinuous region and has been found very helpful for the simulation of cavities and resistive wall. The application of this scheme requires an ultra-relativistic beam and equal DUT cross sections at the entry and exit boundary (e.g., it cannot be applied to simulate a step). In the ultra-relativistic case, if the cross section of the DUT varies at the entry and the exit boundary, the indirect interfaces integration can be used.

Boundary conditions: to be properly defined, depending on the DUT. The CST Wakefield solver allows for different boundary conditions: Electric (tangential component of the electric field $\overrightarrow{E}_t = 0$), Magnetic (tangential component of the magnetic field $\overrightarrow{H}_t = 0$), conductive wall (infinitely thick dissipative wall), periodic and Perfect Matching Layer (PML). For the simulation of the wakes and impedance we typically use Electric or conductive boundary in x and y, and periodic or PML boundaries in z.

Symmetry conditions: when the geometry of the problem makes it possible, to speed up the simulations, symmetry conditions of the fields can be enforced reducing up to a factor 4 the number of mesh cells for Wakefield simulations. This topic is explained in detail in App.A.

3.2 Eigenmode solver

The Eigenmode solver of Microwave Studio (PS), solves Maxwell's equations in frequency domain (FD), using the two available solvers: the Advanced Krylov Subspace method (AKS), and the Jacobi-Davidson method (JDM). The first solver calculates efficiently a number of modes with the lowest resonant frequencies in loss-free structures. The second solver can also be used to calculate non extremal modes at an arbitrary position inside the spectrum. In addition the JDM solver can include even highly lossy materials. The eigenmode solver calculates a finite number of modal field distributions in a closed device. Hexahedral meshes as well as linear and curved tetrahedral meshes are supported[12].

Eigenmode solver: settings
As for the Wakefield solver, a list of the most relevant numerical and physical parameters of the solver is shown:

Mesh Type: For the tetrahedral mesh no choice of the method is required; the external Q-factor can be calculated for structures with waveguide ports attached to the device. Since many structures which require an eigenmode solver have curved surfaces, it is advisable to activate the curved elements for the tetrahedral mesh, since they provide a better approximation of the geometry than linear elements. For the Hexahedral mesh it is possible to choose between the two methods, also in this case the external Q-factor can be calculated for structures with waveguide ports.

Method: The two methods work on a completely different mathematical foundation. The JDM solver can be considered as a more robust solver technology, but the AKS solver may be faster if many modes are to be calculated. Therefore it is recommend the JDM solver only if a small number of modes (e.g. one to five modes) has to be calculated. Otherwise the AKS solver should be used.

Q-factor calculation: The solution of lossy eigenmode problems is a challenging task which implies that the proper consideration of losses will significantly slow down the simulation. Even if the JDM solver is able to directly solve the lossy eigenmode problem, it may sometimes be advisable (especially for very small losses) to first calculate the loss free eigenmode problem and then obtain losses and Q-factors of the device using a perturbation method in the post processing.
The perturbation method requires material losses to be defined before the eigenmode simulation is started. Running the AKS solver will always calculate the loss free problem by simply ignoring the loss definition. The JDM solver by default also ignores the losses when *Consider losses in postprocessing only* is enabled.

Adaptive mesh: The mesh resolution influences the results. The expert system-based mesh generator analyzes the geometry and tries to identify the parts that are critical to the electromagnetic behaviour of the device. The mesh will then automatically be refined in these regions. However, due to the complexity of electromagnetic problems, this approach may not be able to determine all critical domains in the structure. To circumvent this problem, CST MICROWAVE STUDIO features an adaptive mesh refinement which uses the results of a previous solver run in order to improve the expert system's settings.

Chapter 4

EM simulations of the UA9 goniometer and experimental benchmarks

The UA9 collaboration at CERN is investigating how tiny bent crystals could improve beam collimation in modern hadron colliders[13] [14].

Using a tiny bent crystal as a primary collimator, halo protons could be deflected at sufficient large angles and directed into a secondary collimator/absorber away from the beam. In this way the impedance of the total system (bending crystal + collimator/absorber) could be reduced with respect to a collimator/absorber close to the beam[15]. The LHC UA9 piezo goniometer has been designed for this purpose[16].

The goniometer is composed by a rectangular chamber, allocated on the beam line, in which the crystal can be positioned close to the beam, with an angular accuracy of 1 micro-radian[17], by means of a movable holder(see Fig.4.1).

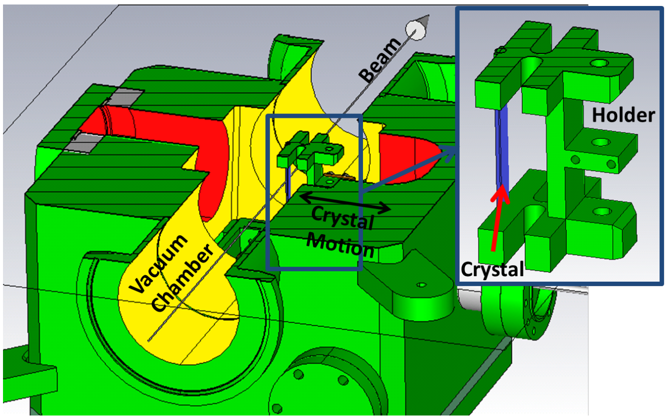

Figure 4.1: UA9 goniometer in operational position: in yellow the vacuum chamber pill-box, in red the holes for parking position and a zoom on the crystal holder area.

Depending on the crystal position two working condition are defined:
operational positions, when the crystal is next to the beam, a condition foreseen to happen just for low-intensity beams (see Fig.4.1);
parking position, when the crystal is hidden to the beam and allocated in a lateral chamber. In this case a masking sector shields the beam pipe.

4.1 Introduction

In this thesis a Finite Element Method (FEM) study of the goniometer in operational position is presented in order to evaluate its impact on the LHC impedance budget. In general, given the strict impedance constraints in LHC, impedance simulations and measurements are part of the procedure to approve and finalize a device installation.

To evaluate the impact on the impedance budget is necessary to study the LHC bunch spectrum. In Fig.4.2 the bunch power spectrum has been evaluated considering a Gaussian profile with $\sigma = 9.75cm$, which is defined as the bunch-length. In LHC the bunch-length varies from $9.75cm$ to $20cm$, the smallest length is the most dangerous because its bunch spectrum is the largest in the machine, as will be explained in the following.

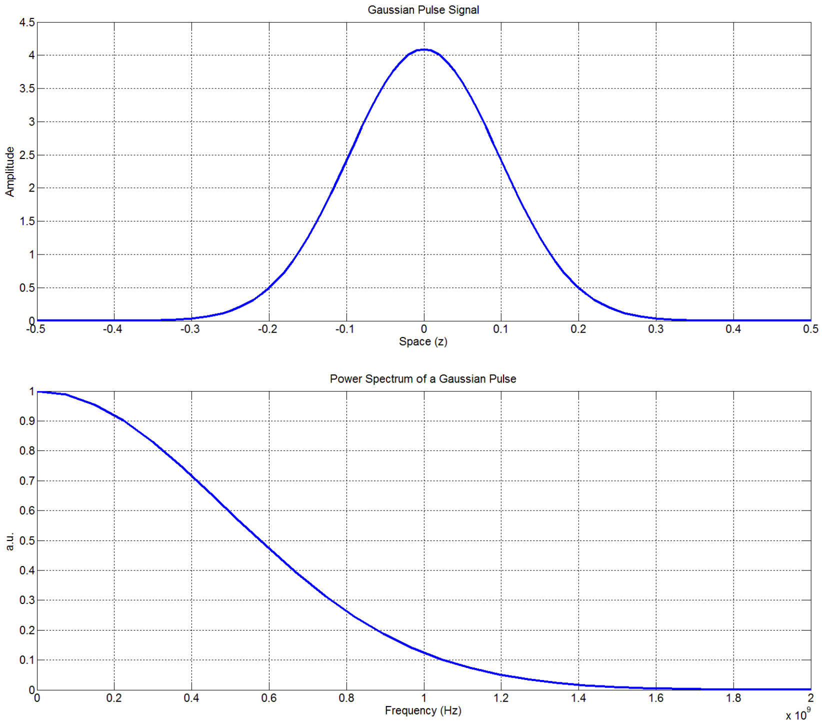

FIGURE 4.2: Gaussian bunch profile for $\sigma = 9.75cm$ and its bunch spectrum.

The relation between the bunch spectrum and the longitudinal impedance $Z_{||}(\omega)$ is evident in the formula 2.10, reported below:

$$\Delta E = \frac{e^2 N_{bunch}^2 \omega_0}{2\pi} \sum_{p=-\infty}^{+\infty} |\bar{\lambda}(p\omega_0)|^2 Re[Z_{\|}(p\omega_0)] \tag{4.1}$$

In Fig.4.2 it is clear that the bunch spectrum components at low-frequency have large amplitude. This means that their weight in the power loss computation, as shown in formula 2.10, will be high.

The final power loss as function of frequency will depend also on the impedance value, in our case the warning frequency threshold for the evaluation of the real part of the longitudinal impedance is $1.2GHz$.

4.2 Simplified models

The code used for the impedance simulations has been CST wakefield solver. For the FEM analysis, the study of the entire structure was not feasible, due to convergence problems caused by the excessively detailed geometry. For this reason it has been decided to start from a simplified structure to which additional elements have been subsequently added step by step. This methodology was good for several reason:

the first is to decrease the number of meshes, consequently reducing both the processing time of the simulation and the memory occupation;

the second reason is to understand the impedance contribution of every single detail of the structure;

the third is to exploit geometrical symmetries of the structure for using the symmetry planes a further reduction of the number of mesh cells (see App.A).

The simulations started from a mechanical model (made by means the CAD Catia) of the goniometer. Than he structure has been simplified keeping the central chamber with the beam pipe apertures, which has been simulated using a simple rectangular pillbox with external cylindrical pipes. Additional elements have been added step by step like the silicon crystal and his PEC holder. Simulations have been also performed taking into account the presence of the external vacuum holes used for housing the crystal in parking position.

4.2.1 Pillbox cavity with and without crystal

The structure in the Fig.4.3 is the simplified model of the UA9 goniometer in operational position, considering only the crystal and the surrounding chamber. It is worth to note that the crystal floats in the vacuum, so this is structure is ideal and cannot exist in reality.

For these simulations the boundaries of the structure are assumed to be PEC, so the losses of the chamber have not been considered, but only the finite conductivity of the crystal (made of polycrystalline silicon). This situation leads to ringing impedance results because the wake potential is not fully vanished (see Sec.3.1).

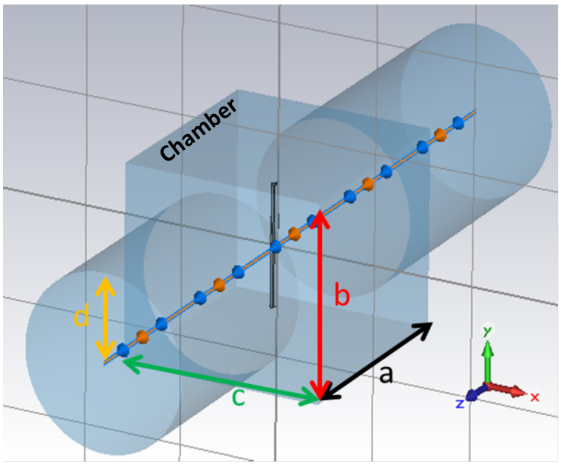

FIGURE 4.3: Simplified structure of UA9 goniometer in operational position with the crystal and the main chamber.

All the simulations in this section have been performed using the geometrical and physical parameters in table 4.1, the dimension of the simplified pillbox are the same of the real chamber. The crystal is centered on the vertical (y) axis, at $z = 0$, at a distance s along the x axis from the center of the structure (see Fig.4.4).

Parameter	Description	Values
a	Pillbox Length	107 mm
b	Pillbox Height	90 mm
c	Pillbox Width	100 mm
d	Pipe Radius	40 mm
s	crystal position	0.5 mm
conductivity	of crystal	2.5 10^{-4} S/m
ϵ	”	11.9
$tg\ \delta$	”	0

TABLE 4.1: Parameter values of the simplified structure.

The first simulations have been performed varying the parameter s. Fig.4.5 shows the longitudinal component of the beam coupling impedance.

Simulations to evaluate the horizontal (Fig.4.6) and vertical (Fig.4.7) component of the beam coupling impedance have been also performed.

Simulations show that all the three components of the coupling impedance do not depend on the crystal position [s = 0.5/1.0/1.5 mm]. The differences are negligible (under *1%*) in all the cases for the chosen position.

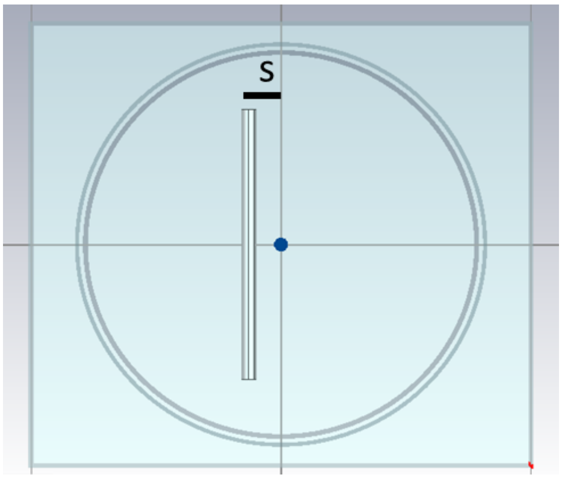

FIGURE 4.4: Explanation of the parameter s, distance of the crystal from the center.

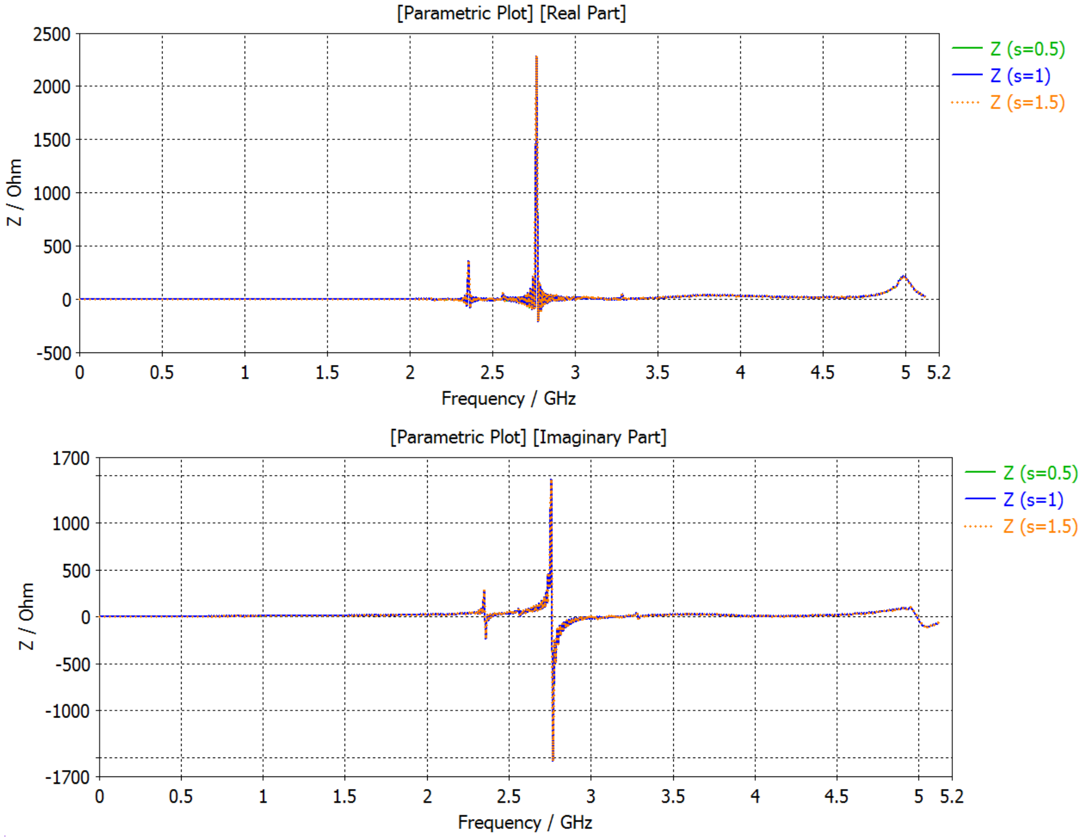

FIGURE 4.5: Real and imaginary parts of longitudinal impedance of the goniometer in operational position, considering the crystal and the chamber, for three different beam-crystal distances s.

In order to understand the influence of the crystal on the impedance, a simulation has been performed considering only the chamber without the crystal, the result is shown in Fig.4.8.

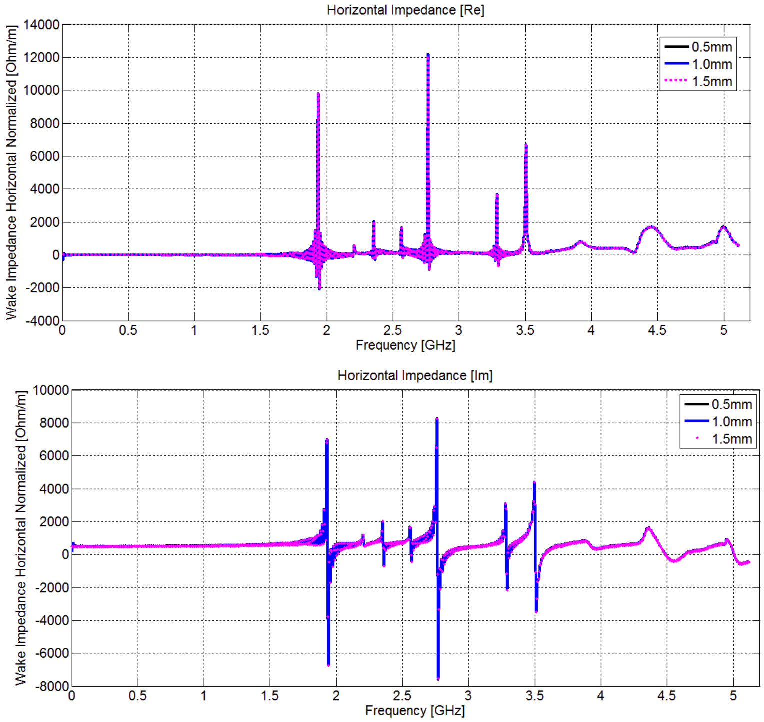

FIGURE 4.6: Real and imaginary parts of horizontal impedance of the goniometer in operational position, considering the crystal and the chamber, for three different beam-crystal distances *s*.

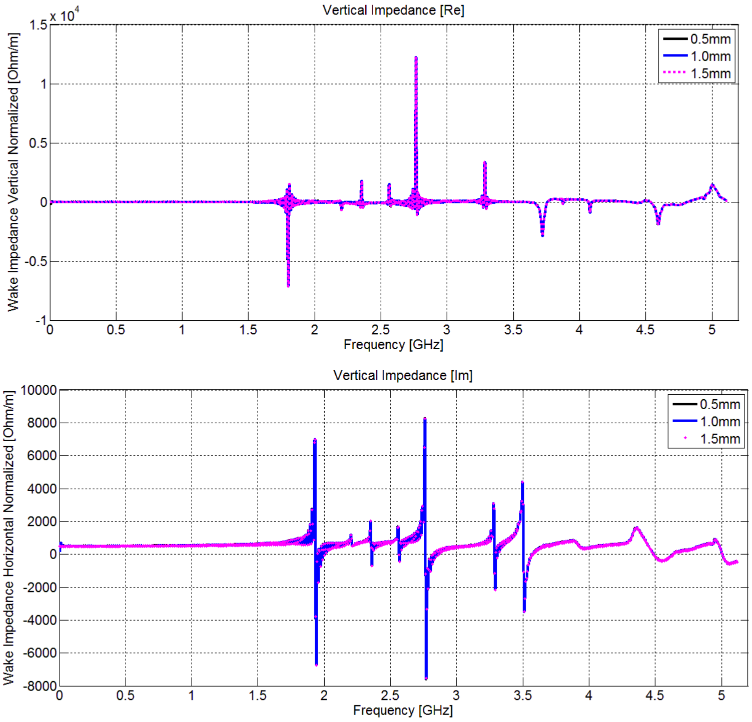

FIGURE 4.7: Real and imaginary parts of vertical impedance of the goniometer in operational position, considering the crystal and the chamber, for three different beam-crystal distances *s*.

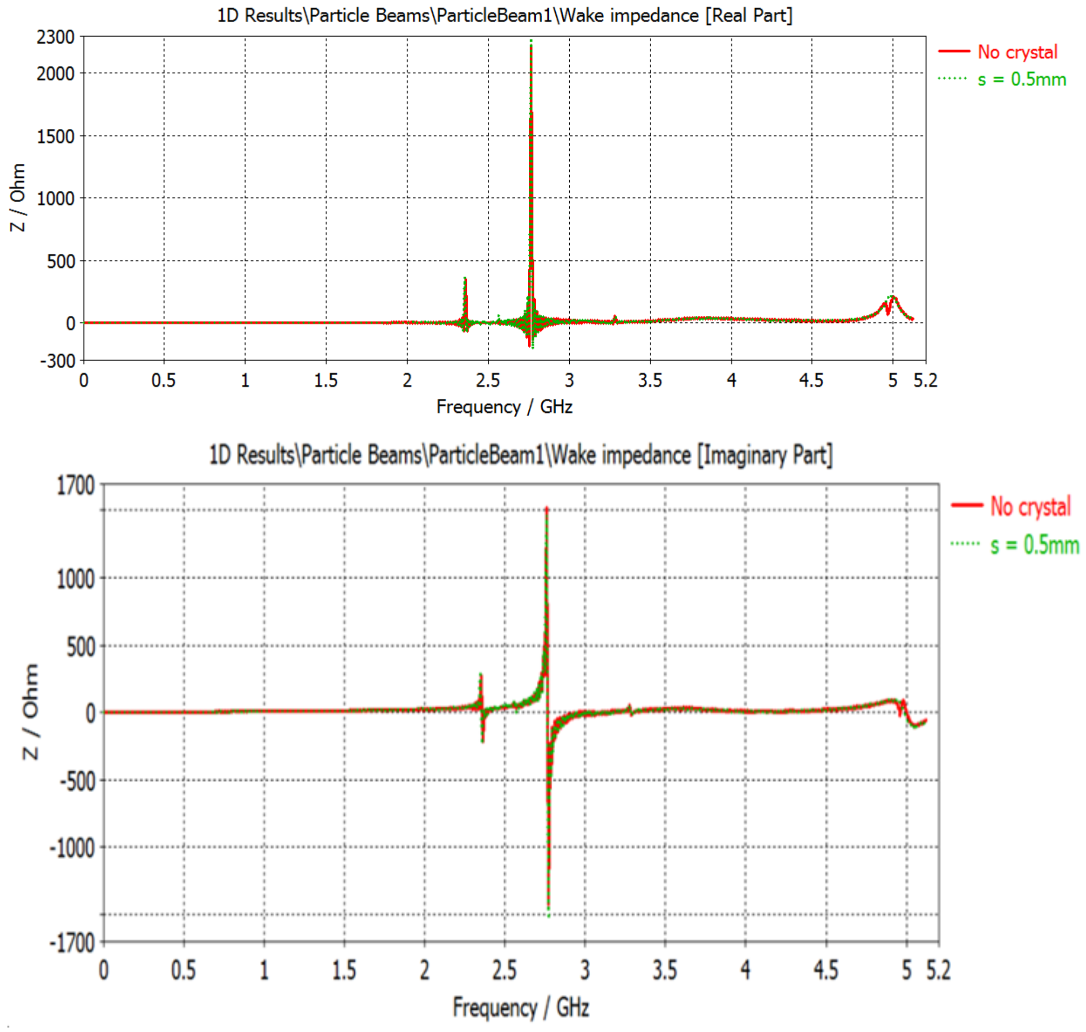

FIGURE 4.8: Comparison of the real and imaginary parts of longitudinal impedance of the goniometer in operational position, with crystal (distance s=*0.5 mm*) and without crystal.

In Fig.4.8 the frequency of the peak is at roughly *2.76GHz*, also by the case without crystal and the difference between the two cases is less than *2.5%*.

This means that the presence of the crystal gives a negligible contribute to the coupling impedance.

The dependence of the coupling impedance on the electromagnetic properties of the crystal has been also investigated.

Crystal	Frequency [GHz]	Long. Impedance [kΩ]
YES	2.355	0.36
NO	2.358	0.35
YES	2.765	2.28
NO	2.765	2.23

TABLE 4.2: Comparison of the impedance peaks in case with and without crystal

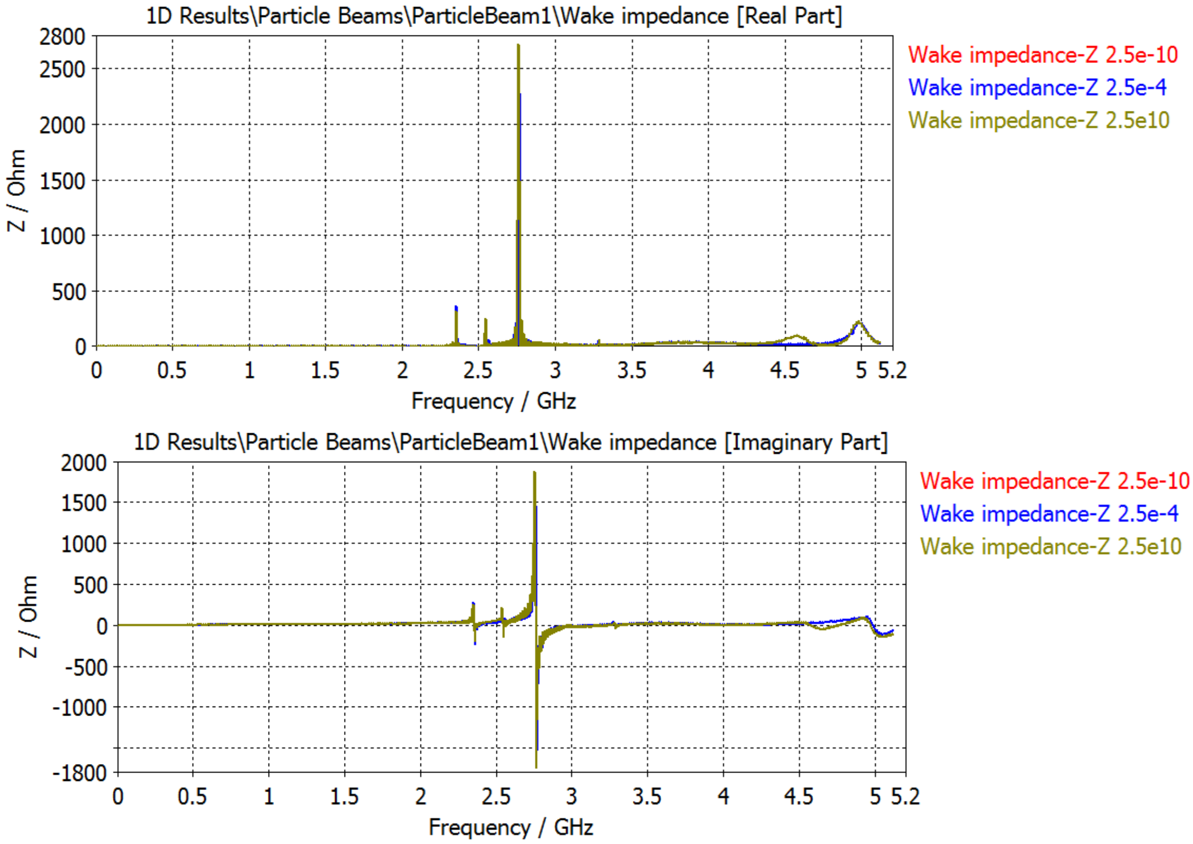

FIGURE 4.9: Real and imaginary parts of longitudinal impedance of the goniometer in operational position, varying the value of the crystal conductivity.

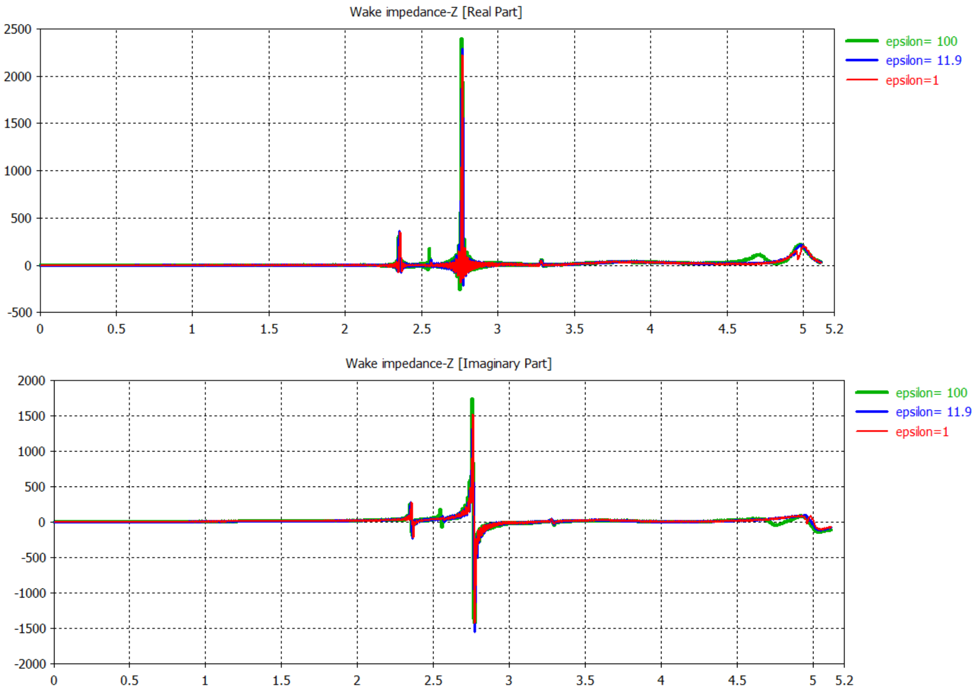

FIGURE 4.10: Real and imaginary parts of longitudinal impedance of the goniometer in operational position, varying the value of the crystal permittivity.

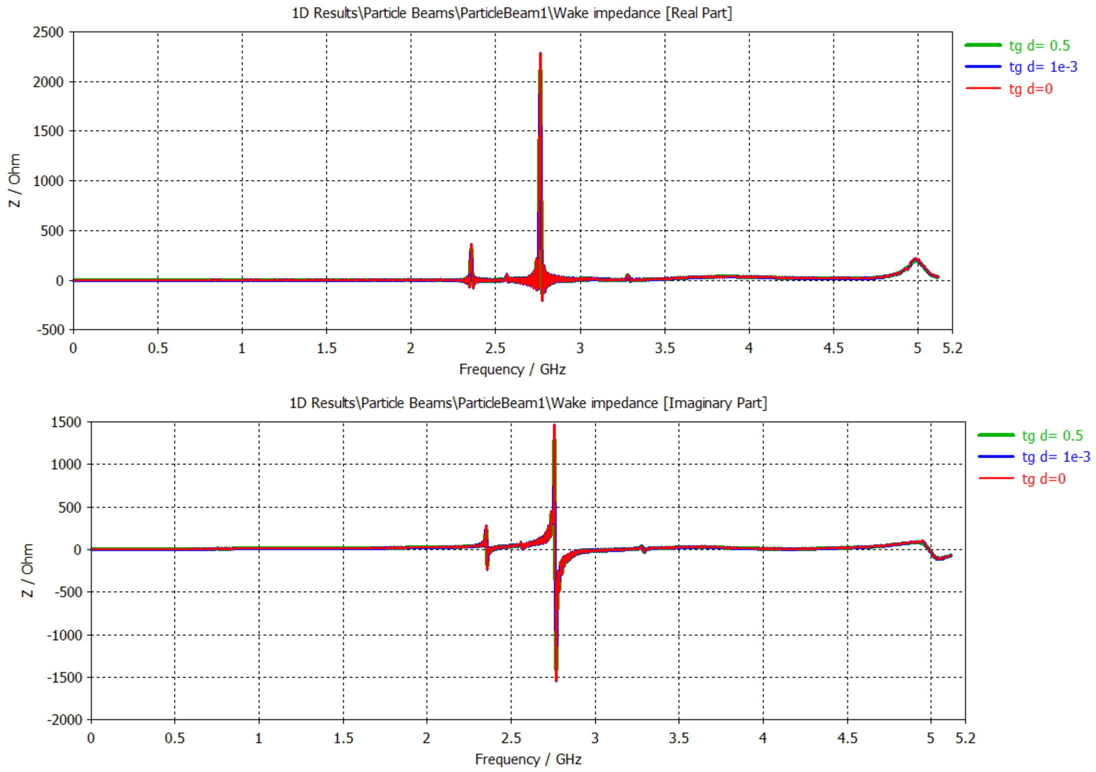

FIGURE 4.11: Real and imaginary parts of longitudinal impedance of the goniometer in operational position, varying the value of the *tg* δ of the crystal.

The results shown in Fig.4.9/4.10/4.11 confirm that the influence of the crystal on coupling impedance value is negligible.

In fact, varying the conductivity value over twenty orders of magnitude, the frequency of the coupling impedance peak values is in a range of less than *2%*, with its amplitude variation in a range of *20%*.

Also varying the permittivity of two orders of magnitude, the frequency variation of the peak is in a range of less than *2%*, with its amplitude variation in a range of less than *10%*.

Changing the *tg* δ in a range [0,0.5], the amplitude variation is less than *8%*.

Simulations considering the crystal with an anisotropic permittivity have been also performed; also in this case the value variations allow to say that the coupling impedance contribution does not depend on the crystal presence.

4.2.2 Pillbox cavity with crystal and holder

The structure in Fig.4.12 is the simplified model of the UA9 goniometer, considering also the PEC holder of the silicon crystal. Also in this case the crystal and its holder float in the vacuum.

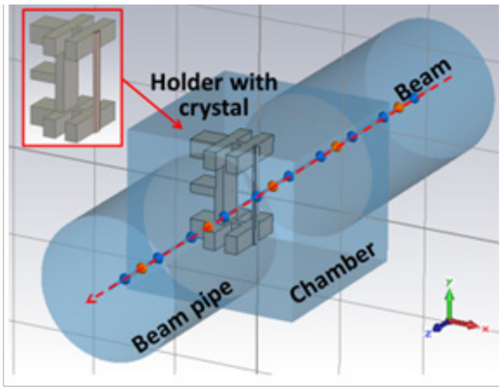

FIGURE 4.12: Simplified structure of UA9 goniometer in operational position with the crystal, its PEC holder and the main chamber.

The simulations performed show a peak at *1.63GHz* (see Fig.4.13). Making a zoom on the peak (Fig.4.14) is possible to see the frequency shift varying the positions of the crystal and therefore of the holder.

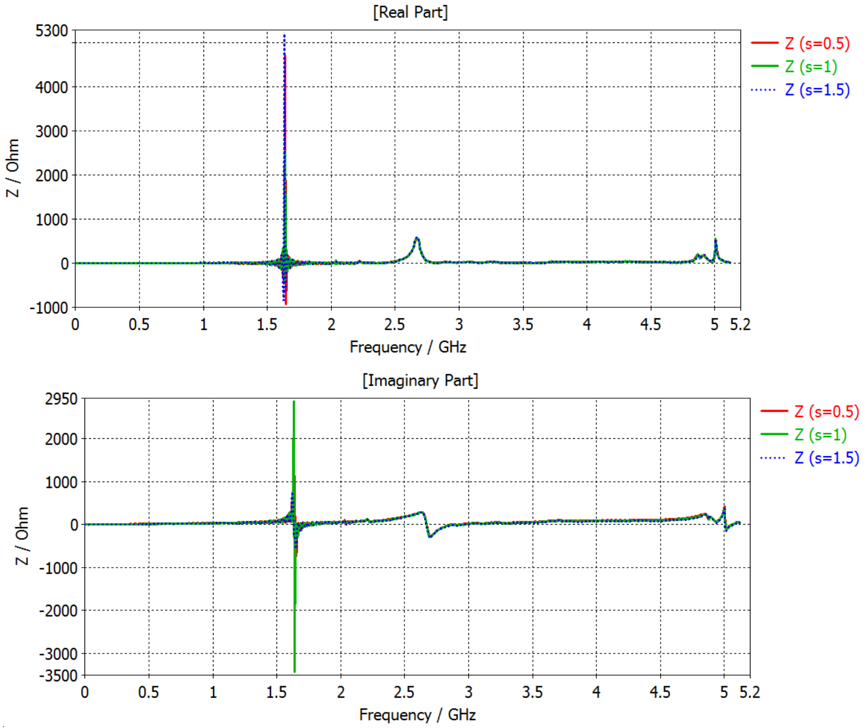

FIGURE 4.13: Real and imaginary parts of longitudinal impedance of the goniometer in operational position, with the crystal, its PEC holder and the chamber, for three different beam-crystal distances *s* (see Fig.4.4).

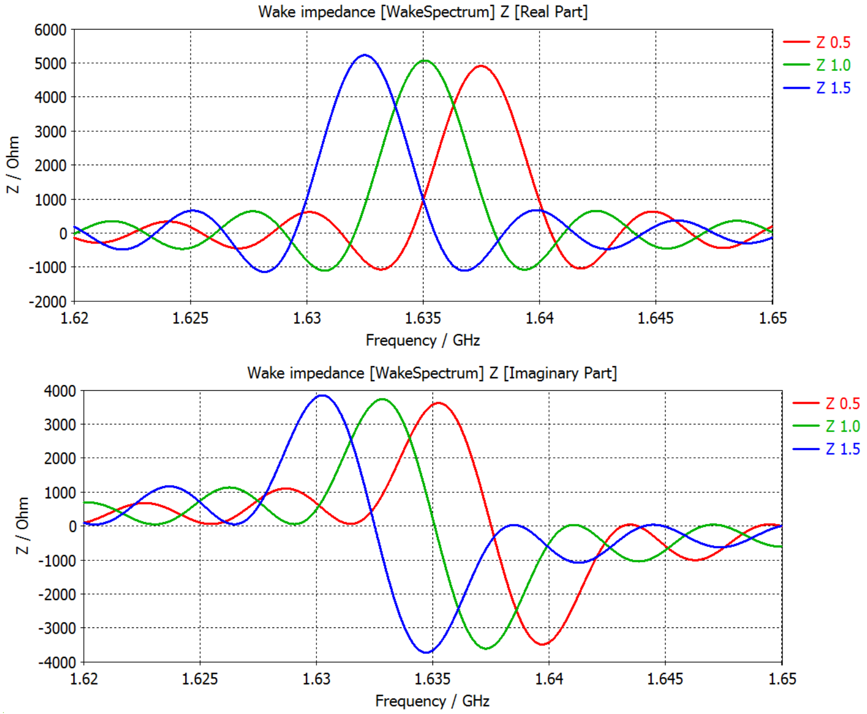

FIGURE 4.14: Zoom in a range $[1.62,1.65]GHz$ ot the real and imaginary parts of longitudinal impedance of the goniometer in operational position, with the crystal, its PEC holder and the chamber, for three different beam-crystal distances s.

In Tab.4.3 the results are shown in detail. Increasing the distance from the center there is a shift to the low frequency of few MHz and the value of the real part of the longitudinal impedance increase.

s [mm]	Frequency [GHz]	Long. Impedance [kΩ]
0.5	1.637	4.90
1.0	1.635	5.07
1.5	1.632	5.23

TABLE 4.3: Impedance peaks values varying beam-crystal distances s.

The longitudinal impedance has been evaluated and compared, shown in Fig.4.15, for the structure with and without the holder.
Is possible to see the values of the peaks in Tab.4.4. The largest peak shown at $2.76GHz$ without the holder appears at low frequency, $1.64GHz$, considering the holder.

Holder	Frequency [GHz]	Long. Impedance [kΩ]
YES	1.638	4.72
NO	2.355	0.36
YES	2.672	0.57
NO	2.765	2.28

TABLE 4.4: Comparison of the impedance peaks in case with and without holder

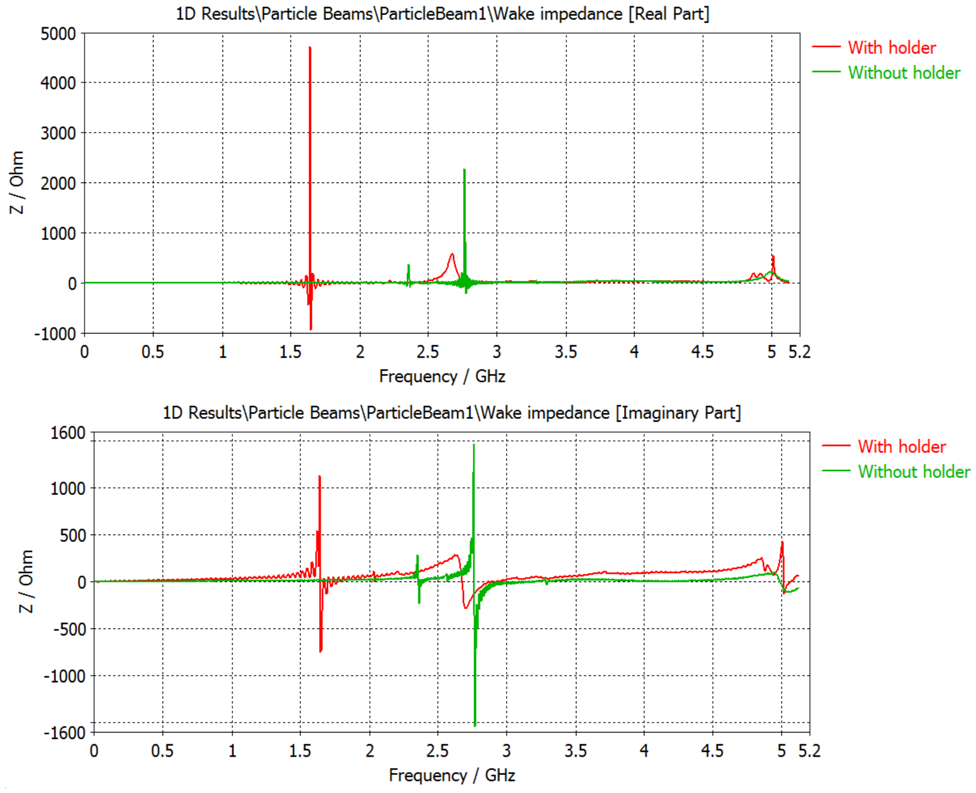

FIGURE 4.15: Comparison of the real and imaginary parts of longitudinal impedance of the goniometer in operational position.The red line is considering the crystal (distance s=*0.5 mm*) with the holder and the green line is without the holder.

4.2.3 Pillbox cavity with holes

A further step in the simulation analysis was to consider the two external vacuum holes used to housing the crystal in the configuration of parking position (see Fig.4.16). This configuration is closer to reality.

All the geometrical parameters of these two external holes are reported in Tab.4.5

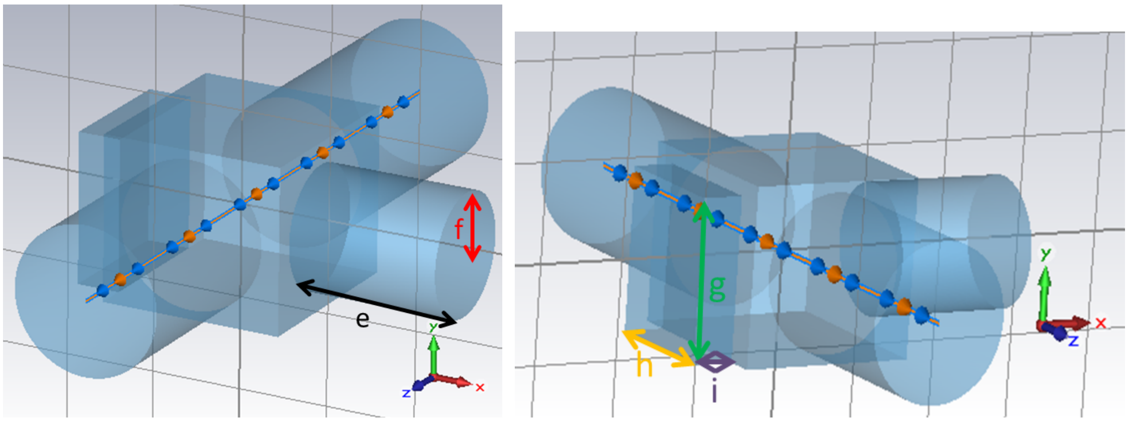

FIGURE 4.16: Simplified structure of UA9 goniometer in operational position considering the external holes and the main chamber.

Parameter	Description	Values
e	Length circ. hole	82 mm
f	Radius circ. hole	33 mm
g	Height rect. hole	82 mm
h	Length rect. hole	74.4 mm
i	Width rect. hole	23.5 mm

Table 4.5: Parameter values of the simplified structure with holes

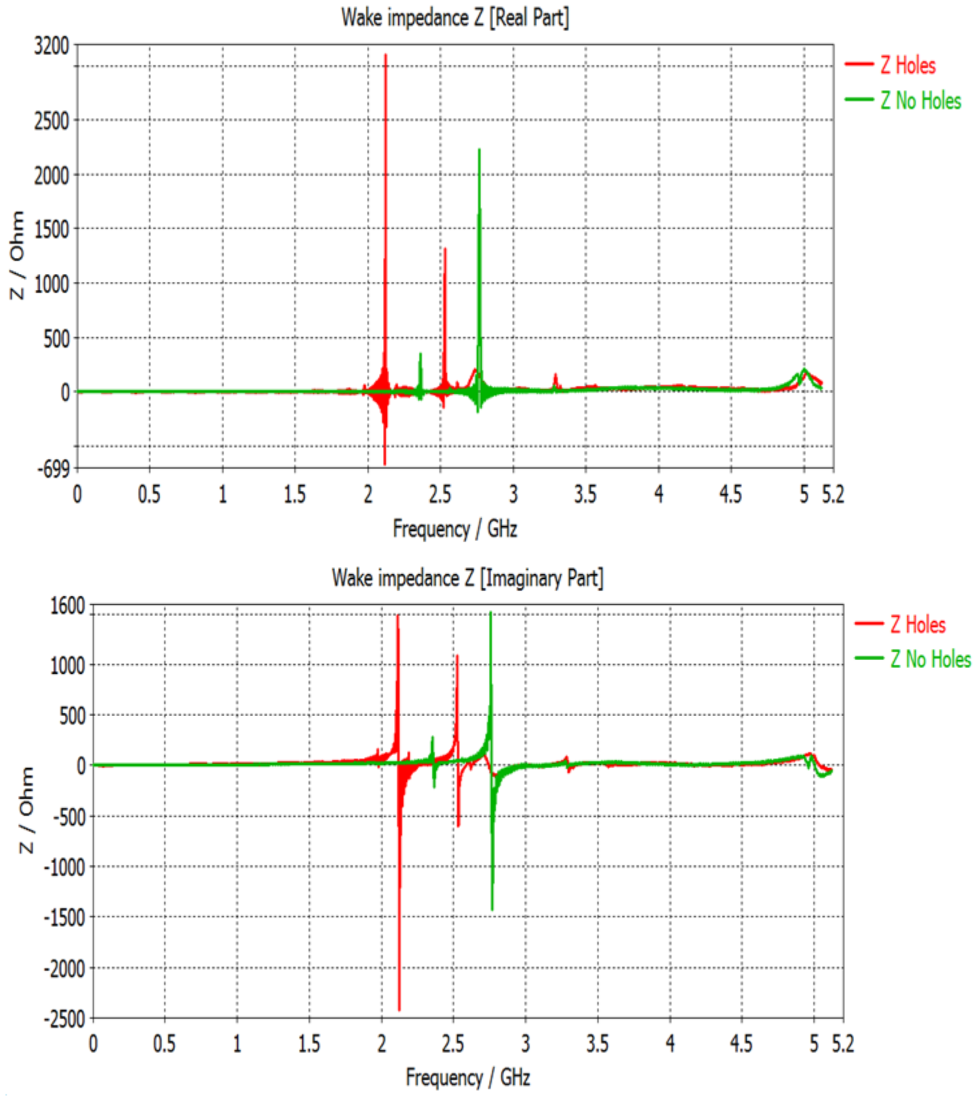

Figure 4.17: Comparison of the real and imaginary parts of longitudinal impedance of the goniometer in operational position, considering the external holes and without holes

Fig.4.17 shows the results considering the simplified structure without the crystal: the red line is relative to the case with the external vacuum holes and the green line is relative to the case without the external holes (already seen in Fig.4.8).

In Tab.4.6 the values of the real part of the impedance peaks are shown. The presence

Holes	Frequency [GHz]	Long. Impedance [kΩ]
YES	2.119	3.10
NO	2.360	0.35
YES	2.529	1.32
NO	2.765	2.23
YES	2.755	0.20

TABLE 4.6: Comparison of the impedance peaks in case with and without external holes

of the new volumes varies the impedance spectrum. It can be notice that the peaks at roughly 2.76GHz is always present because due to the beam-pipe cut-off.

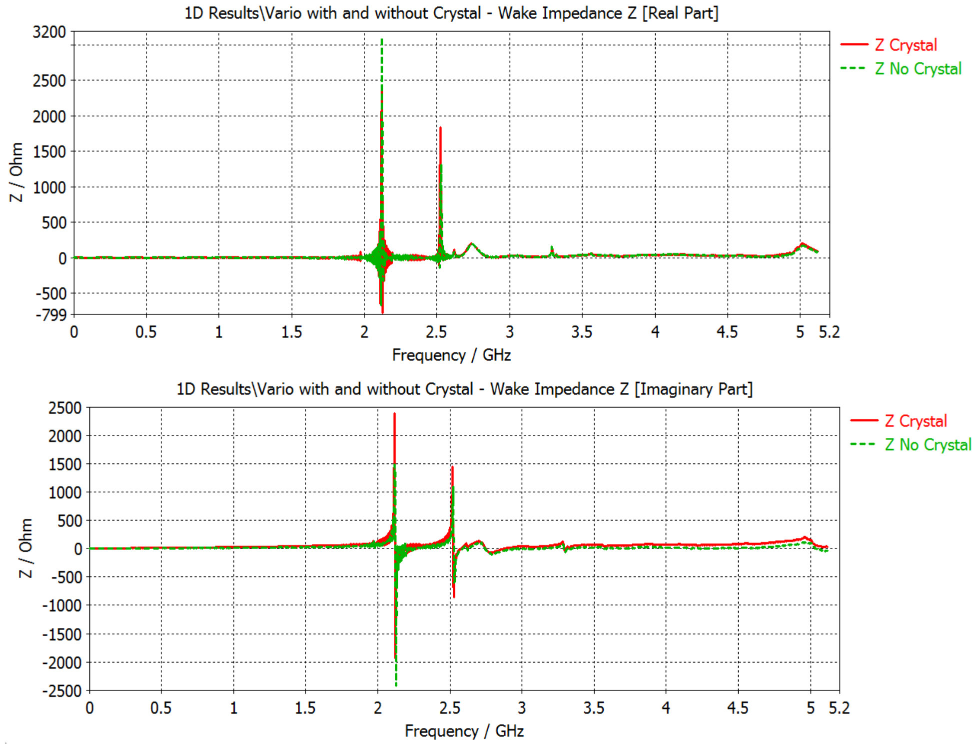

FIGURE 4.18: Comparison of the real and imaginary parts of longitudinal impedance of the goniometer in operational position, considering the crystal (distance s=*0.5 mm*) and without crystal

Holes	Crystal	Frequency [GHz]	Long. Impedance [kΩ]
YES	YES	2.119	2.38
YES	NO	2.119	3.10
YES	YES	2.524	1.83
YES	NO	2.529	1.32
YES	YES	2.755	0.21
YES	NO	2.755	0.20

TABLE 4.7: Comparison of the impedance peaks in case with and without crystal

As last case, the crystal has been added to the simplified structure with the external holes(see Fig.4.18). The red line shows the results considering the crystal and the green line is relative to the case without the silicon crystal.

In Tab.4.7 are shown the values of the real part of the impedance peaks. The peaks at *2.12GHz* for both cases confirm that the presence of the crystal is negligible for the evaluation of the longitudinal impedance.

The real and the imaginary part of the longitudinal impedance considering also the PEC holder of the crystal in Fig.4.19 are shown.

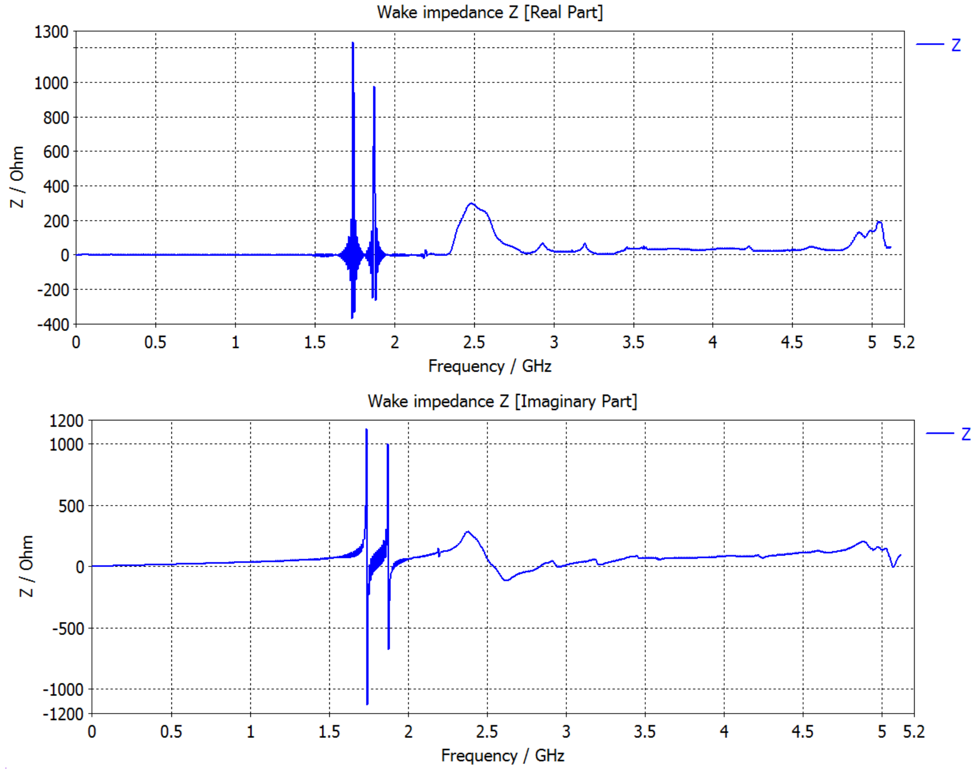

FIGURE 4.19: Real and imaginary parts of longitudinal impedance of the goniometer in operational position, considering the crystal (distance s=*0.5 mm*), the holder and the external holes.

The Fourier transform relation between the wake potential and the coupling impedance is underlined in Fig.4.20, in fact the distance between the two wake potential minimum is *2.2248m* corresponding to a variation of frequency of $\Delta f = 135MHz$, which is exactly the distance between the two peaks for this case (see Ch.2).

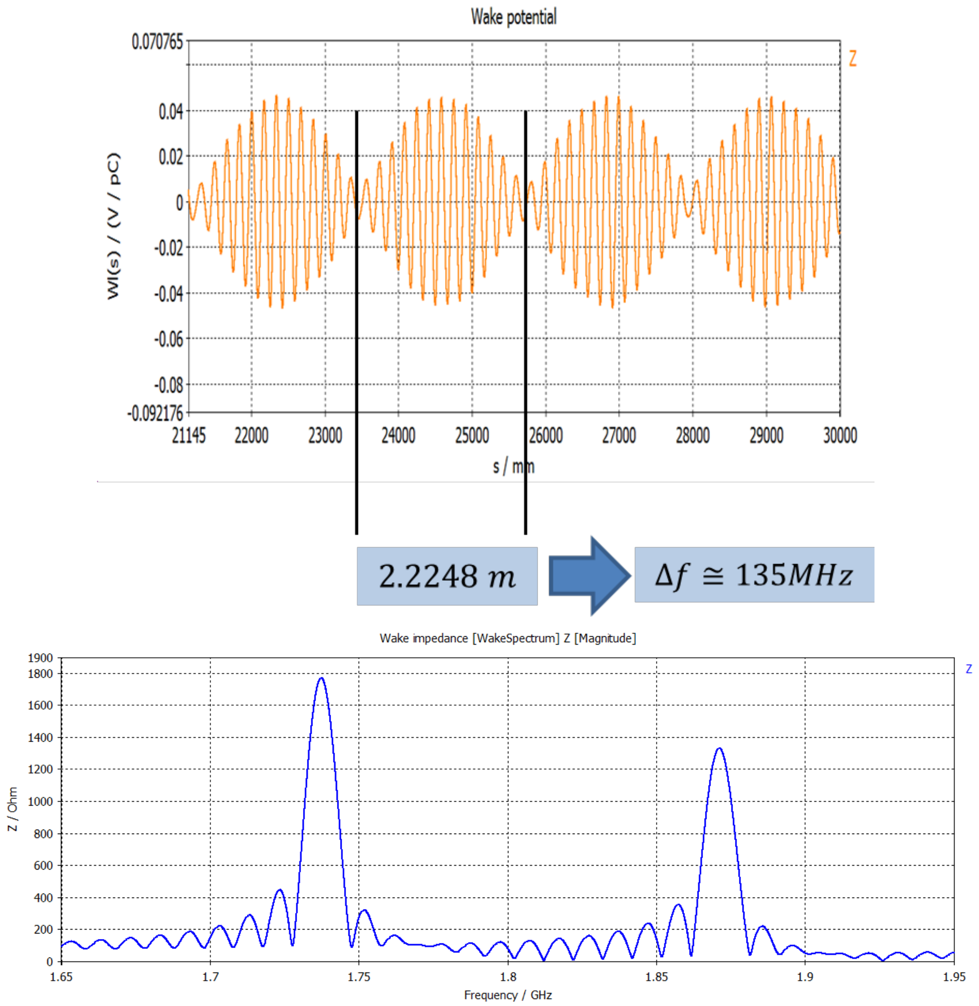

FIGURE 4.20: Zoom on the wake potential (top) and on the real part of longitudinal impedance (bottom) of the goniometer in operational position, considering the crystal (distance s=$0.5\ mm$), the holder and the external holes.

4.3 CST detailed geometry and comparison with wire measurements

As previously mentioned at the beginning of this chapter, in the impedance budget calculation of the UA9 goniometer great attention has to be put in studying the structure EM behaviour below $1GHz$. Bench measurements based on the stretched wire method can be useful in order to identify structure modes at frequency below $1GHz$. Measurements have been conducted on the goniometer in operational position without silicon crystal and holder. A resistance has been used to match the characteristic impedance of the coaxial line formed by the wire and the beam pipe to the impedance of the VNA coaxial.

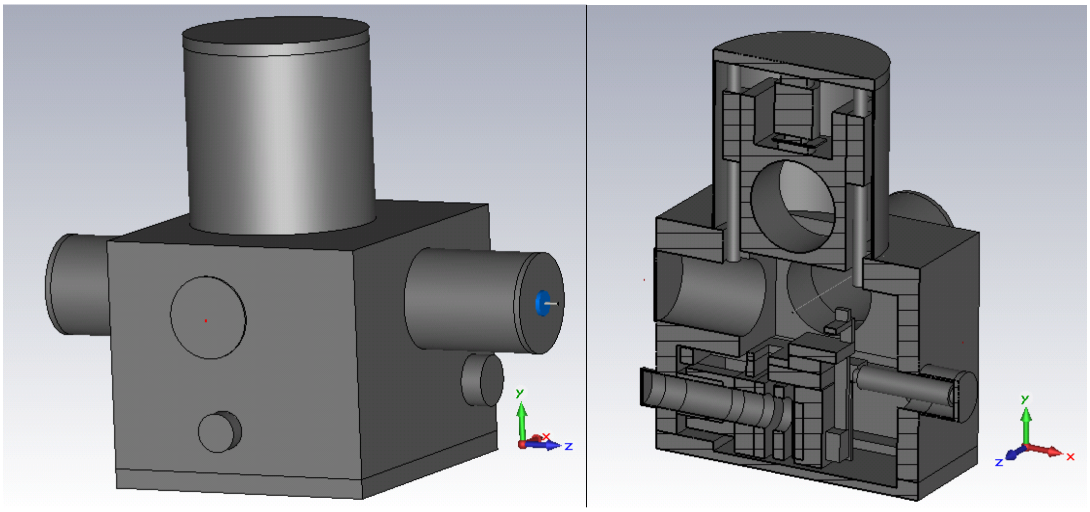

FIGURE 4.21: CST detailed geometry, complex structure.

Electromagnetic simulations of this structure have been performed trying to be as close as possible to the measurement setup (see Fig.4.21).

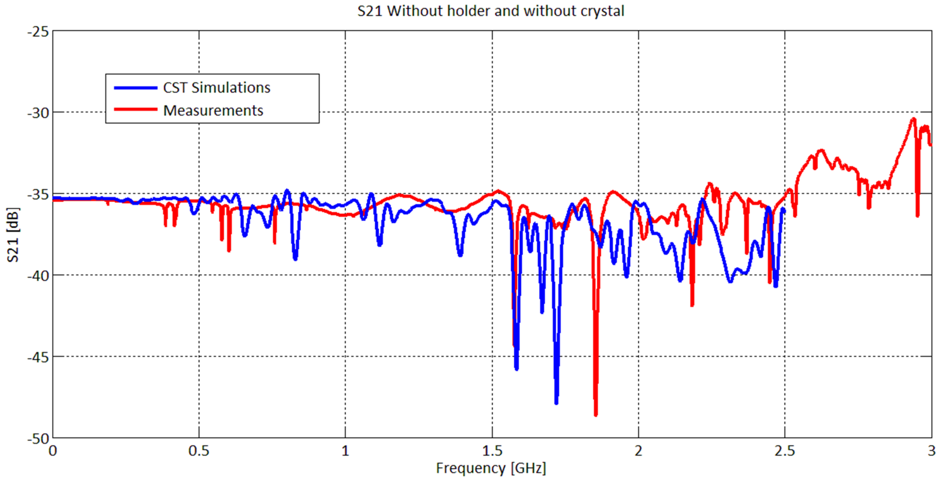

FIGURE 4.22: S_{21} measurements (red line) and CST time domain simulations (blue line) of the complete structure without crystal and holder.

The results of the simulations in the time domain (see Fig.4.22) are not in very good agreement with the measurements. The reason of the discrepancy between measurements and simulations is because the simulated model can not be as accurate as the real model and also the meshes can not perfectly fit the simulated structure because of the complexity of the geometry. However, the simulations show resonant modes below *1GHZ* in a good qualitative agreement with measurements. Moreover, simulations of the structure have also been performed without the wire with the eigenmode solver and the results confirm the presence of few impedance peaks below *1GHz*.

Chapter 5

Beam coupling impedance measurements below the pipe cut-off frequency: numerical investigations

5.1 Introduction

The Cap.4 clearly shows that numerical modelling is problematic for structures with non-elementary geometries or composed by materials with unknown or complex electromagnetic properties.
In this chapter a benchmark on a numerical/experimental method has been performed to evaluate the beam coupling impedance even for non-elementary structures. For the validation of this method a pillbox has been characterized comparing analytical formulas, numerical results and experimental measurements.

The measurements have been conducted by the accelerators physics group at INFN of Naples, inside the experiment IMCA, in order to characterize accelerator elements below the pipe cut-off frequency.

Ideally measurements of beam coupling impedances of a device should be done by exciting the device with the beam itself[18]. However, in most cases this solution is not feasible and one must resort to bench measurement techniques in which the beam is simulated by a current pulse flowing through a wire stretched along the beam axis. For beam coupling impedance evaluations, the wire method (WM) is a common and appreciated choice. This technique was proposed in the first half of the 70's, based on intuitive

considerations. By means of WM, Faltens et al.[19] measured the wall contributions to the beam coupling impedance. M. Sands and J. Rees (1974)[20] measured the energy loss of a stored beam to a cavity due to the higher mode excitation. The method of Sands and Rees based on the measurement of the scattering matrix of the device under test (DUT) requires a complex numerical manipulation to obtain the beam coupling impedance only of the DUT[20]. An improved method of measurement that requires less manipulation and gives a clear response was proposed by V. G. Vaccaro[21].
Since many years it has become customary to use the coaxial wire method to measure the beam coupling impedance of accelerator devices. Nevertheless, the results obtained from wire measurements might not entirely represent the solution of our initial problem, because the presence of the stretched wire perturbs the EM boundary conditions. The most evident consequence of the presence of another conductive medium in the center of the DUT is the fact that it artificially allows TEM propagation through the device, with zero cut-off frequency. The presence of a TEM mode among the solutions of the EM problem will have the undesired effect to cause additional losses during the measurement.Theoretical studies about the validity limits of the Sands and Rees method in relation to the presence of the central wire that simulates the beam can be found in Ref.[22].
However, the mode analyzed in this study is above the cut-off frequency of the beam chamber. For modes below this frequency, due to the TEM propagation introduced by the wire, the WM is found to provide inaccurate results, as investigated in Ref.[23] comparing the impedance with and without a wire for a Copper pillbox, by means of the Mode Matching Technique.

To overcome the problems of the WM measure of the beam coupling impedance, the accelerators physics group at INFN of Naples has developed a new method using small antennas to perform the measurements of the resonant frequencies and the relative Q below the cut-off frequency of sample pill-box cavity.

The idea behind this experimental method is that the energy released by the beam in the resonant cavity have to go back again to the same beam. Below the cut-off frequency no energy can flow out within the beam. Therefore, the real part of the beam coupling impedance must be zero far from resonance frequency because no energy is released into the chamber or is lost by ohmic dissipation into the device. However it is expected that the real part of the impedance is different from zero, when the cavity has finite conductivity walls, because the superficial current on the walls dissipates a certain amount of energy: the power exchange between the cavity and the beam is no longer balanced. At the cavity resonance frequencies is possible to see a significant component of beam coupling impedance.

The experimental method with small antennas has been developed for structure electromagnetic characterization below the cut-off. The coupling impedance in this range of frequencies is calculated by means of the numerical/experimental method introduced in this thesis. The idea is to combine the resonance frequency and Q factor measured and with R_{sh}/Q simulated in order to disentangle the coupling Impedance below the cut-off.

5.2 Example of application: a pillbox cavity

This chapter shows the simulation, measurements and analytical calculations performed on the Pill-Box shown in Fig.5.1, placed at the INFN laboratory of Naples.

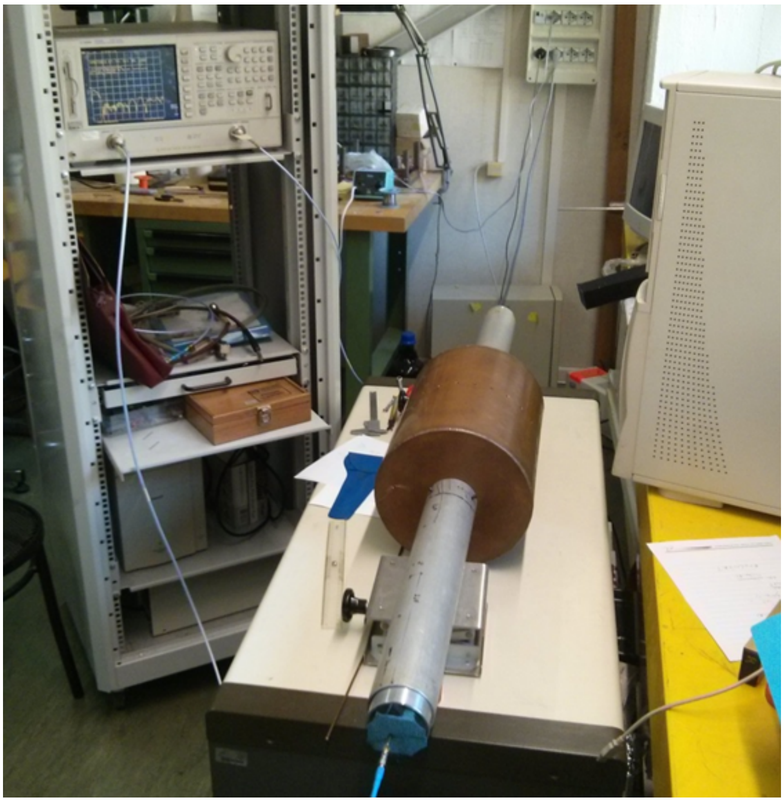

FIGURE 5.1: Pill-box.

The dimensions and EM characteristic of the pillbox cavity are reported in Fig.5.2 and Tab.5.1

The cut-off frequency of the system for the longitudinal mode is:

$$f_{cut-off} = \frac{\rho_{1,0} \cdot c}{2\pi b} = \frac{2.405 \cdot 310^{8}}{2\pi 0.034} = 3.377GHz \tag{5.1}$$

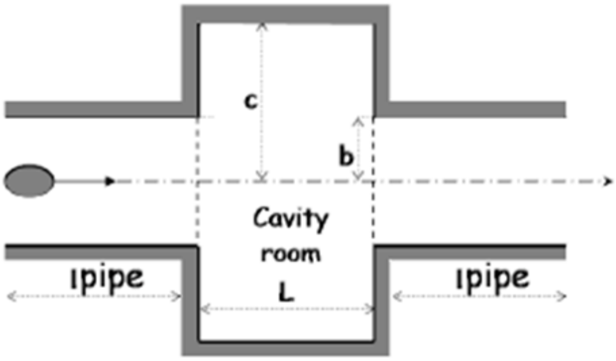

FIGURE 5.2: Pill-box geometry.

Parameter	Description
R	125 mm
b	34 mm
L	375 mm
lpipe	600 mm
conductivity	5.96 10^7 S/m

TABLE 5.1: Pillbox parameters.

where $\rho_{1,0}$ is the zero of the Bessel function;
c is the speed of light in vacuum;
b is the radius of the external pipes.

5.2.1 Analytical model of resonant frequencies and quality factors

A cylindrical cavity resonator can be constructed from a section of circular waveguide shorted at both ends.

The geometry of a cylindrical cavity is shown in Fig.5.3. The solution is simplified by beginning with the circular waveguide modes,which already satisfy the necessary boundary conditions on the wall of the circular waveguide. The transverse electric fields (E_ρ, E_ϕ) of the TE_{nm} or TM_{nm} circular waveguide mode can be written as:

$$E_t(\rho,\phi,z) = e(\rho,\phi)[A^+ e^{-j\beta_{nm}z} + A^- e^{j\beta_{nm}z}] \tag{5.2}$$

where $e(\rho,\phi)$ represents the transverse variation of the mode, and A^+ and A^- are arbitrary amplitudes of the forward and backward travelling waves. The propagation constant of the TE_{nm} mode is:

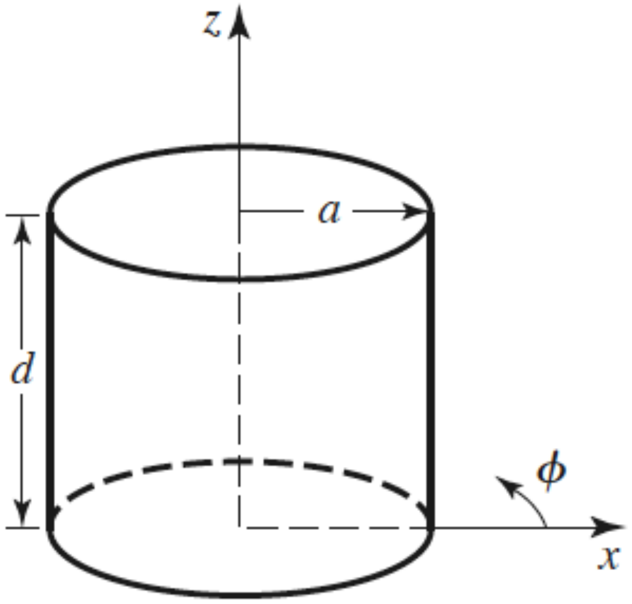

FIGURE 5.3: A cylindrical resonant cavity.

$$\beta_{nm} = \sqrt{k^2 - \left(\frac{p'_{nm}}{a}\right)^2} \tag{5.3}$$

while the propagation constant of the TM_{nm} mode is:

$$\beta_{nm} = \sqrt{k^2 - \left(\frac{p_{nm}}{a}\right)^2} \tag{5.4}$$

where $k = \omega\sqrt{\mu\epsilon}$, p_{nm} and p'_{nm} are the m-zeros of the Bessel function of n order and of its derivative and a is cavity radius.
In order to have $E_t = 0$ at $z = 0, d$, we must choose $A^+ = A^-$, and $A^+ = sin(\beta_{nm})d = 0$, or $\beta_{nm}d = l\pi$, for $l = 0, 1, 2, 3, \dots$, which implies that the waveguide must be an integer number of half-guide wavelength long. Thus, the resonant frequency of the TE_{nm} mode is:

$$f_{nml} = \frac{c}{2\pi\sqrt{\mu_r\epsilon_r}}\sqrt{\left(\frac{p'_{nm}}{a}\right)^2 + \left(\frac{l\pi}{d}\right)^2} \tag{5.5}$$

and the resonant frequency of the TM_{nm} mode is:

$$f_{nml} = \frac{c}{2\pi\sqrt{\mu_r\epsilon_r}}\sqrt{\left(\frac{p_{nm}}{a}\right)^2 + \left(\frac{l\pi}{d}\right)^2} \tag{5.6}$$

The dominant TE mode is the $TE_{1,1,1}$ mode, while the dominant TM mode is the $TM_{0,1,0}$ mode [24].

At frequencies near resonance, a microwave resonator can usually be modelled by a parallel RLC lumped-element equivalent circuit. Some of the basic properties of these circuits are here reviewed.
The input impedance of the parallel RLC resonant circuit, shown in Fig.5.4, is: The

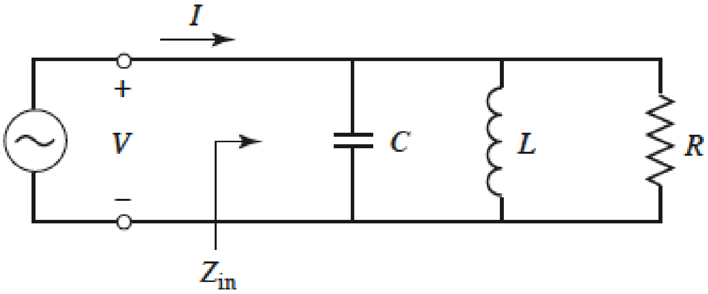

Figure 5.4: A parallel RLC resonant circuit.

input impedance of the parallel RLC resonant circuit, shown in Fig.5.4, is:

$$Z_{in} = \left(\frac{1}{R} + \frac{1}{j\omega L} + j\omega C \right)^{-1} \tag{5.7}$$

and the complex power delivered to the resonator is[24]:

$$P_{in} = \frac{1}{2} V I^* = \frac{1}{2} Z_{in} |I|^2 = \frac{1}{2} |V|^2 \frac{1}{Z_{in}^*} = \frac{1}{2} |V|^2 \left(\frac{1}{R} + \frac{1}{j\omega L} + j\omega C \right) \tag{5.8}$$

The power dissipated by the resistor, R, is:

$$P_{loss} = \frac{1}{2} \frac{|V|^2}{R} \tag{5.9}$$

the average electric energy stored in the capacitor, C, is:

$$W_e = \frac{1}{4} |V|^2 C \tag{5.10}$$

and the average magnetic energy stored in the inductor, L, is:

$$W_m = \frac{1}{4} |I_L|^2 L = \frac{1}{4} |I_L|^2 \frac{1}{\omega^2 L} \tag{5.11}$$

where I_L is the current through the inductor. Then the complex power in 5.8 can be rewritten as:

$$P_{in} = P_{loss} + 2j\omega(W_m - W_e) \tag{5.12}$$

Similarly, the input impedance can be expressed as:

$$Z_{in} = \frac{2P_{in}}{|I|^2} = \frac{P_{loss} + 2j\omega(W_m - W_e)}{\frac{1}{2}|I|^2} \tag{5.13}$$

As in the series case, resonance occurs when $W_m = W_e$. Then from 5.13 and 5.9 the input impedance at resonance is:

$$Z_{in} = \frac{P_{loss}}{\frac{1}{2}|I|^2} = R \tag{5.14}$$

which is a purely real impedance. From 5.10 and 5.11, $W_m = W_e$ implies that the resonant frequency, ω_0, can be defined as:

$$\omega_0 = \frac{1}{\sqrt{LC}} \tag{5.15}$$

Another important parameter of a resonant circuit is its Q, or *quality factor*, which is defined as:

$$Q = \omega\frac{\text{average energy stored}}{\text{energy loss/second}} = \omega\frac{W_m + W_e}{P_{loss}} \tag{5.16}$$

Thus Q is a measure of the loss of a resonant circuit—lower loss implies a higher Q. Resonator losses may be due to conductor loss, dielectric loss, or radiation loss, and are represented by the resistance, R, of the equivalent circuit. An external connecting network may introduce additional loss. Each of these loss mechanisms will have the effect of lowering the Q. The Q of the resonator itself, disregarding external loading effects, is called the unloaded Q, denoted as Q_0. From the definition and the results in 5.9, 5.10 and 5.11, the unloaded Q of the parallel resonant circuit can be expressed as:

$$Q_0 = \omega_0\frac{2W_{in}}{P_{loss}} = \frac{R}{\omega_0 L} = \omega_0 RC \tag{5.17}$$

since $W_m = W_e$ at resonance. This result shows that the Q of the parallel resonant circuit increases as R increases.

Near resonance, the input impedance of 5.7 can be simplified using the series expansion $\frac{1}{1+x} \simeq 1 - x + \ldots$. Again letting $\omega = \omega_0 + \Delta\omega$, where $\Delta\omega$ is small, allows 5.7 to be rewritten as:

$$Z_{in} \simeq \frac{R}{1 + 2jQ_0\Delta\omega/\omega_0} \tag{5.18}$$

since $\omega_0^2 = 1/LC$. When $R =\infty$ 5.18 reduces to:

$$Z_{in} = \frac{1}{j2C(\omega - \omega_0)} \tag{5.19}$$

The effect of loss can be accounted for by replacing ω_0 in this expression with a complex effective resonant frequency:

$$\omega_0 \leftarrow \omega_0 \left(1 + \frac{j}{2Q_0}\right) \tag{5.20}$$

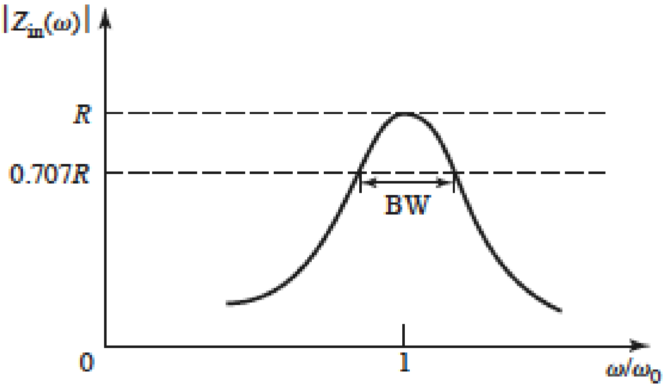

FIGURE 5.5: A parallel RLC resonator response, input impedance magnitude versus frequency.

Figure 5.5 shows the behaviour of the magnitude of the input impedance versus frequency. The half-power bandwidth edges occur at frequencies ($\omega/\omega_0 = BW/2$) such that:

$$|Z_{in}|^2 = \frac{R^2}{2} \tag{5.21}$$

which, from 5.18, implies that:

$$BW = \frac{1}{Q_0} \tag{5.22}$$

For the studied pill-box the Q factor, taking into account of the losses due to the cavity aperture is:

$$Q_{m,l} = \frac{\omega_{m,l} Z_0 \sigma \delta_{m,l} L_c}{2c_l(L + c\epsilon_l)} = \frac{k_{m,l} Z_0 \sigma \delta_{m,l} L_c}{2(L + c\epsilon_l)} \tag{5.23}$$

f is the resonance frequency;
c_l is the light speed in air;
Z_0 is the characteristic air impedance;

σ is the copper electric conductivity;

$\delta_{m,l}$ is the skin depth;

μ is the air magnetic permeability;

L is the cavity length;

c is the cavity radius;

$\epsilon_l = \begin{cases} 1 & \text{if } l = 0 \\ 2 & \text{if } l \neq 0 \end{cases}$

5.2.2 Analytical calculation of the beam coupling impedance by using the mode matching technique

The Mode Matching method, represents the EM fields in one of the finite sub-domains as sum of eigenmodes whose unknown coefficients form an infinite vector [25][26]. A number of functional equations are obtained by matching the tangential component of the fields on the domains boundaries. By means of the Ritz-Galerkin method [27], each functional equation is transformed in an infinite set of equations which link the unknown vectors.

The idea of the Mode Matching technique is to divide the given geometry in a series of sub-regions in which the wave equation is separable. The fields and the modes have to be evaluated for each sub-region. Subsequently, these Modal expansions are forced to satisfy the boundary conditions among these sub-regions.

In this section the expressions for the electromagnetic field decomposition in a closed volume are shown. The derived equations are the basis for the Mode Matching method. Given a volume V, enclosed in an ideal surface $S = S_E \cup S_H$, with S_E perfect electric, and S_H perfect magnetic boundary surfaces, the scattered electromagnetic fields E and H may be decomposed by means of the Helmholtz theorem in summation of irrotational and solenoidal modes which constitute a complete set of orthonormal functions [25][26]. It is possible to write[28]:

$$\overline{E} = \sum_n \mathbf{V}_n \overline{e}_n + \sum_n \mathbf{F}_n \overline{f}_n \tag{5.24}$$

$$\overline{H} = \sum_n \mathbf{I}_n \overline{h}_n + \sum_n \mathbf{G}_n \overline{g}_n \tag{5.25}$$

where $\overline{e}_n$ and $\overline{h}_n$ are solenoidal and $\overline{f}_n$ and $\overline{g}_n$ irrotational orthonormal eigenvectors. Table 5.2 resumes a set of eigenvectors and the relative differential equations and boundary conditions they satisfy ($\widehat{n}_0$ is the unit vector normal to S pointing internally the volume). Since the eigenvectors are determined by the geometry of the structure under

study, the problem reduces to finding the coefficients $\mathbf{V}_n$, $\mathbf{F}_n$, $\mathbf{I}_n$, $\mathbf{G}_n$.
This can be done by imposing the continuity of the EM field on the boundary surface S. In this condition one must also take into account also the impressed field generated by the sources.

On S_E, because of the homogeneous boundary condition, which is an intrinsic property of the eigenmodes, it is not possible to perform tout court the matching of the electric field. Analogously this happens on S_H for the magnetic field. This difficulty can be overcome by resorting to a procedure which will be described in the following. Let E be the given imposed electric field on the surface S. Resorting to simple algebra, the quantity $\nabla \cdot (\overline{E} \times \overline{h}_n^*)$ can be written as:

Eigenvector	In V	On $S = S_E \cup S_H$
$\overline{e}_n$	$\nabla \times \overline{e}_n = k_n \overline{h}_n$	$\begin{cases} \widehat{n}_0 \times \overline{e}_n = 0 & \text{on } S_E \\ \widehat{n}_0 \cdot \overline{e}_n = 0 & \text{on } S_H \end{cases}$
$\overline{f}_n = \nabla \phi_n$	$\nabla^2 \phi_n + \mu_n^2 \phi_n = 0$	$\begin{cases} \phi_n = 0 & \text{on } S_E \\ \partial \phi_n / \partial n = 0 & \text{on } S_H \end{cases}$
$\overline{h}_n$	$\nabla \times \overline{h}_n = k_n \overline{e}_n$	$\begin{cases} \widehat{n}_0 \times \overline{h}_n = 0 & \text{on } S_E \\ \widehat{n}_0 \cdot \overline{h}_n = 0 & \text{on } S_H \end{cases}$
$\overline{g}_n = \nabla \psi_n$	$\nabla^2 \psi_n + \nu_n^2 \psi_n = 0$	$\begin{cases} \psi_n = 0 & \text{on } S_E \\ \partial \psi_n / \partial n = 0 & \text{on } S_H \end{cases}$

TABLE 5.2: Eigenvector equations.

$$\nabla \cdot (\overline{E} \times \overline{h}_n^*) = \overline{h}_n^* \cdot (\nabla \times \overline{E}) - \overline{E} \cdot (\nabla \times \overline{h}_n^*) \tag{5.26}$$

The Maxwell's equation for E and 5.24 are used into the RHS, then integrated on the volume V. Applying the divergence theorem and exploiting the orthonormality of the eigenmodes, the following expression is obtained:

$$\int_{S_E} (\overline{E} \times \overline{h}_n^*) \cdot \widehat{n}_0 dS = -jkZ_0 \mathbf{I}_n - k_n \mathbf{V}_n \tag{5.27}$$

where $\widehat{n}_0$ is the unitary vector pointing inward the volume V boundaries, Z_0 is the characteristic impedance and $k = \omega/c$ the propagation constant in vacuum.
Doing the same for the quantity $\nabla \cdot (\overline{e}_n^* \times \overline{H})$, the equation obtained is:

$$\int_{S_E} (\overline{e}_n^* \times \overline{H}) \cdot \widehat{n}_0 dS = k_n \mathbf{I}_n - jkY_0 \mathbf{V}_n \tag{5.28}$$

with $Y_0 = 1/Z_0$. Solving the system of 5.27 and 5.28 allows us to get the coefficients I_n and V_n:

$$\mathbf{I}_n = \frac{1}{k^2 - k_n^2}(jkY_0 \int_{S_E} (\overline{E} \times \overline{h}_n^*) \cdot \widehat{n}_0 dS - k_n \int_{S_H} (\overline{e}_n^* \times \overline{H}) \cdot \widehat{n}_0 dS) \tag{5.29}$$

$$\mathbf{V}_n = \frac{1}{k^2 - k_n^2}\left(jkZ_0 \int_{S_H} (\overline{e}_n^* \times \overline{H}) \cdot \widehat{n}_0 dS + k_n \int_{S_E} (\overline{E} \times \overline{h}_n^*) \cdot \widehat{n}_0 dS\right) \tag{5.30}$$

Analogously is possible to proceed for the irrotational fields obtaining:

$$\mathbf{G}_n = j\frac{Y_0}{k} \int_{S_E} (\overline{E} \times \overline{g}_n^*) \cdot \widehat{n}_0 dS \tag{5.31}$$

$$\mathbf{F}_n = -j\frac{Z_0}{k} \int_{S_E} (\overline{H} \times \overline{f}_n^*) \cdot \widehat{n}_0 dS \tag{5.32}$$

The results of the above procedure may appear contradictory. On S_E, for example, the use of the eigenmodes which satisfy homogeneous boundary conditions is imposed: one might be tempted to infer that the expansion coefficients should vanish. There is, indeed, no contradiction:
the result of the LHS of 5.29-5.32 is obtained integrating on the volume V a positive definite function, while the result of the RHS is obtained integrating on the surface S the "imposed" field $\overline{E}$. However, such an expansion will only be non-uniformly convergent. This behaviour will require some caution when truncating the expansion.

The longitudinal impedance can be calculated by means of

$$Z_{\|}(\omega) = -\frac{1}{Q} \int_{-\infty}^{\infty} dz e^{\frac{j\alpha_b z}{b}} E_z \tag{5.33}$$

Dividing the calculation for the different sub-domains the longitudinal impedance value can be disentangled.For a more detailed description, please refer to[28]

5.2.3 Comparison among CST simulations, analytical formula and Mode Matching results

CST eigenmode simulation (described in sec.3.2) has been performed on the Pill-box described in Tab.5.1; the simulated structure is represented in Fig.5.6, where all the parameters are closer as possible as to the reality.

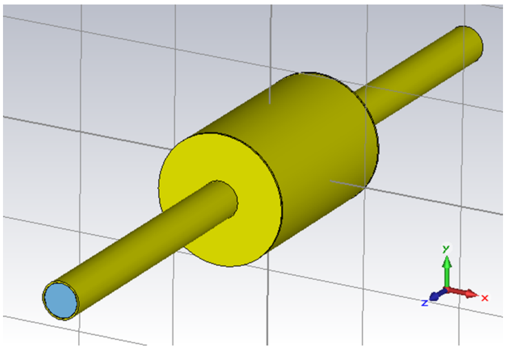

FIGURE 5.6: CST model of the Pill-box (see the Fig.5.1).

In Tab.5.3 the values of resonance frequencies and Q factors are shown: the CST simulations with eigenmode solver, the analytic formulas (see the eq.5.6 and 5.23), and the mode matching method (see the sec.5.2.2) are compared.

The values of the resonant frequencies reported are below the lowest cut-off frequency of the pipe modes $f_{cut-off} = 3.377 GHz$ (see the eq.5.1). So far our attention has been restricted only in this range of frequency.

The values of Tab.5.3 have been reported in Fig.5.7.

f^{TM}_{nml}	CST f_r $[GHz]$	CST Q factor	Analytic f_r $[GHz]$	Analytic Q factor	M.M. f_r $[GHz]$	M.M Q factor
$0,1,0$	0.92154	44139	0.91857	43655	0.92161	43472
$0,1,1$	1.00783	36800	1.00188	36414	1.00794	36518
$0,1,2$	1.22267	40023	1.21810	40152	1.22276	40221
$0,1,3$	1.51433	44418	1.51121	44722	1.51441	44751
$0,1,4$	1.84673	48993	1.84493	49414	1.84679	49484
$0,2,0$	2.11736	73339	2.10852	66033	2.11746	66378
$0,2,1$	2.16507	59549	2.14613	53295	2.16525	51700
$0,1,5$	2.20316	53947	2.20086	53971	2.20326	54080
$0,2,2$	2.27612	57170	2.25519	54633	2.27636	55547
$0,2,3$	2.44496	57729	2.42608	56665	2.44519	57237
$0,1,6$	2.56980	57813	2.56978	58319	2.56985	58351
$0,2,4$	2.66260	59526	2.64686	59187	2.66281	59864
$0,2,5$	2.91678	62078	2.90618	62019	2.91693	61615
$0,1,7$	2.94695	61724	2.94682	62451	2.94702	62542

TABLE 5.3: Comparison between CST eigenmode simulation, analytic formula and mode matching method.

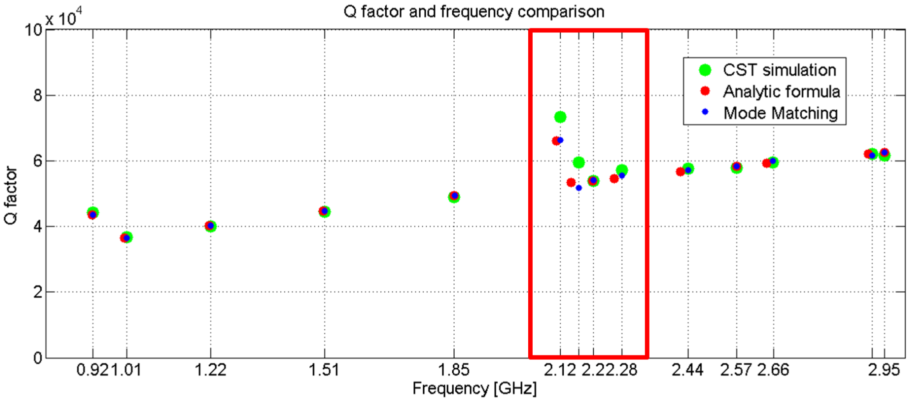

FIGURE 5.7: Comparison between CST eigenmode simulation, analytic formula and mode matching method.

There is a very good agreement between the three method, except in a small frequency band which is framed in Fig.5.7. This region is magnified in Fig.5.8. Even if the discrepancies are rather small both in frequency and amplitude, it is worthwhile to try give a plausible interpretation of this phenomenon. In this frequency band may exist two TM modes, one denoted by the mode number $(2, 1, 2)$ and the second one by $(2, 1, 3)$.

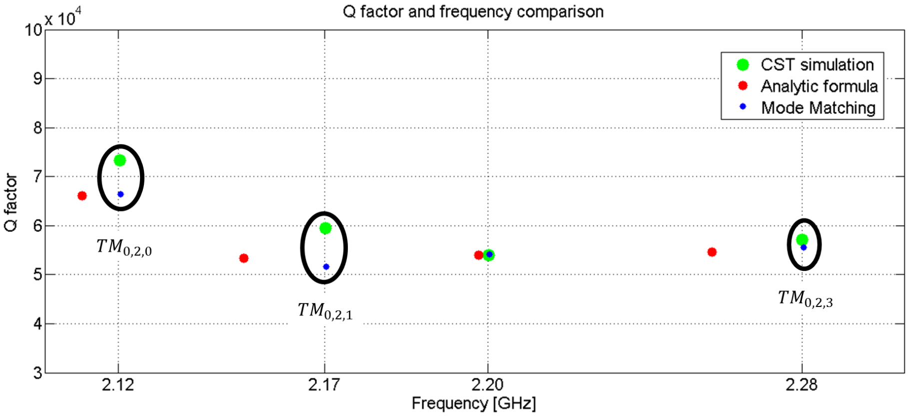

FIGURE 5.8: Frame region magnified of Fig.5.7.

They both exhibit the longitudinal electric field component vanishing on the axis. It is plausible to guess that the presence of this modes have a negative influence on the simulation results.

5.2.4 Measurements with probes

Experimental measurements have been carried out using an Agilent E5071C Network Analyzer in the laboratory of accelerator physics at INFN in Naples. This device measures the S-parameters of a 2-port network.
With pill-box configuration, shown in Fig.5.9, it has been possible to perform the measures of the resonant frequencies and the Q factors of each mode.

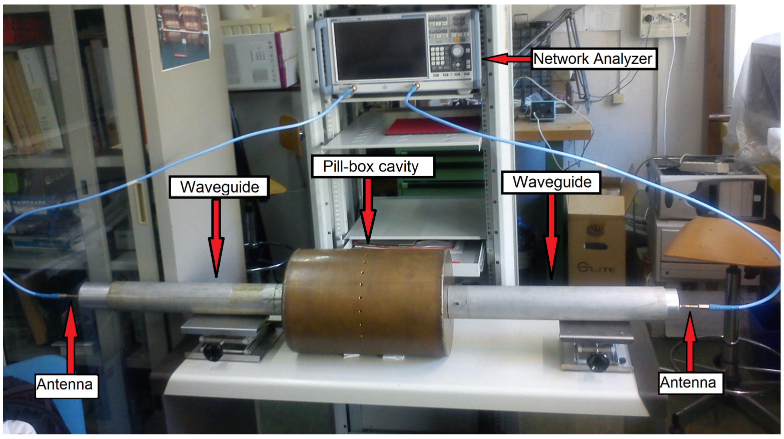

FIGURE 5.9: Pill-box with antennas connected to the VNA.

Different measurements have been performed at various distances of the antennas from the cavity pill-box entrance by using a telescopic structure as shown in Fig.5.9: it has to be noted that moving away the antenna from the pill-box entrance it is possible to

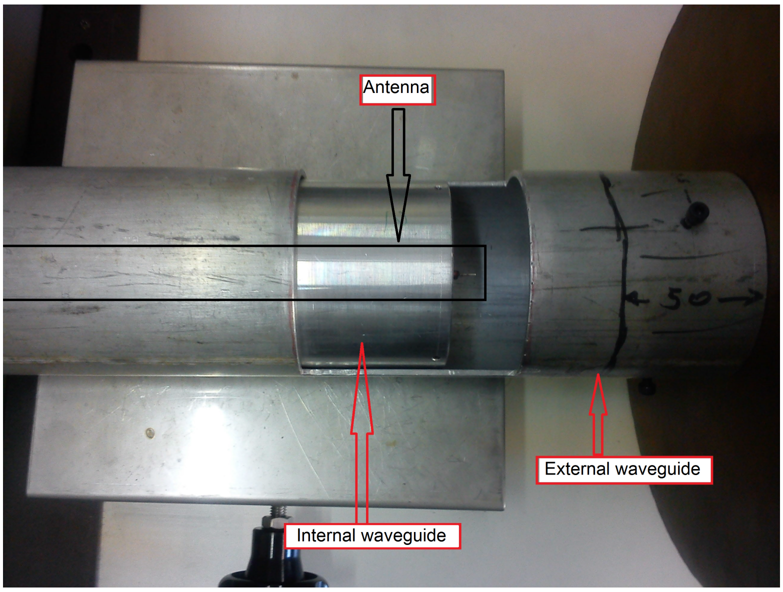

FIGURE 5.10: Detail of the internal waveguide with antenna inside.

reduce the coupling with electric field.

Once performed the calibration, S-parameters and Q factor have been measured for each resonance frequency at distances $4,0cm$, $5,1cm$, $6,0cm$ $7,0cm$ e $8,0cm$ from the cavity. The measures have been performed with 1601 points with an $IF\ Bandwidth = 10Hz$. The formula used to disentangle the Q factor of the cavity will be not reported because awaiting to be published.

5.2.4.1 Measurements of resonant frequencies and quality factors

The measurements described in the section 5.2.4 are reported in Tab.5.4:

f_{nml}^{TM}	Measured f_r $[GHz]$	Measured Q factor	Q factor error ±
$0,1,0$	0.921	43265	2352
$0,1,1$	1.007	35425	2138
$0,1,2$	1.220	38231	2305
$0,1,3$	1.509	42594	2622
$0,1,4$	1.839	46317	2939
$0,2,0$	2.117	66463	7619
$0,2,1$	2.164	53327	2667
$0,1,5$	2.194	54253	2273
$0,1,6$	2.557	59908	2624

TABLE 5.4: Measurements of resonant frequency and Q-factor with the antennas.

The standard deviation of the errors of the Q factor is between 5% and 6% except for the mode $TM_{0,2,0}$. The problem of this mode, as already seen for the simulations, is the

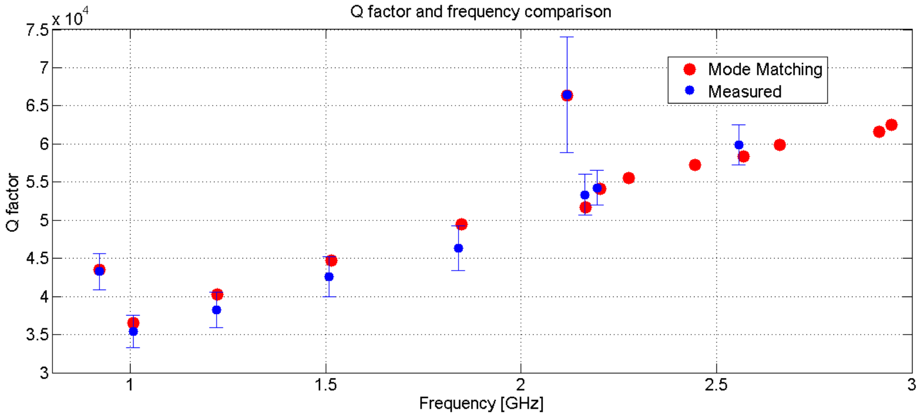

FIGURE 5.11: Comparison between mode matching method and measurements.

presence of an additional $TM_{2,1,2}$ resonance peak at the frequency of $2,113GHz$ which affects the measure with a consequent increase of the standard deviation.
For the modes $TM_{0,2,2}$, $TM_{0,2,4}$, $TM_{0,2,5}$ and $TM_{0,1,7}$, already seen using CST, analytical formula and Mode matching technique, have not been possible to perform the measurements.

5.3 An hybrid numerical/experimental method to compute the beam coupling impedance

The method with antennas does not still allow to measure the value of the coupling impedance below the cut-off frequency.
Taking into account that for resonant cavities it is also convenient to define the shunt impedance, a figure of merit that is independent of the excitation level of the cavity and measures the effectiveness of producing an axial voltage V_0 for a given power dissipated. The shunt impedance R_{sh} of a cavity is defined by:

$$R_s = \frac{V_0^2}{P} \tag{5.34}$$

In an accelerating cavity we are really more interested in maximizing the particle energy gain per unit power dissipation. The peak energy gain of a particle occurs when $\phi = 0$, and is $\Delta W_{\phi=0} = qV_0T$. Consequently, we define an effective shunt impedance of a cavity as

$$R_{sh} = \left[\frac{\delta W_{\phi=0}}{q}\right]^2 \frac{1}{P} = \frac{[V_0T]^2}{P} = R_sT^2 \tag{5.35}$$

This parameter measures the effectiveness per unit power loss for delivering energy to a particle. For a given field both $V_0 = E_0 L$ and P increase linearly with cavity length, as do both R_{sh} and R_s.
Another useful parameter is the ratio of effective shunt impedance to Q, often called R_{sh} *over* Q,

$$\frac{R_{sh}}{Q} = \frac{[V_0 T]^2}{\omega U} \tag{5.36}$$

We see that R_{sh}/Q measures the efficiency of acceleration per unit stored energy at a given frequency. This ratio is useful because it is a function only of the cavity geometry and it is independent of the surface properties that determine the power losses[29].

That is why the numerical/experimental method has been introduced. The idea is to combine the Q factor measured with antenna method and the R_{sh}/Q simulated using CST eigenmode solver in order to evaluate the shunt resistance R_{sh} for each resonant mode with following formula:

$$Q_m(f_n) \cdot \left(\frac{R_{sh}(f_n)}{Q(f_n)} \right)_{sim} = R_{sh}(f_n) \tag{5.37}$$

Is interesting to notice that the value of $Q_{measured}$ depends even on the EM properties of the material inside the structure (roughness, conductivity, etc.). On the other hand the ratio $R_{sh}/Q_{simulated}$ depends only on the geometry structure if in the structure is not present a strongly dispersive material (e.g. ferrite).
A Lorentzian fit has been used to connect the values of resonance frequency, Q factor and shunt resistance to the coupling impedance value, using the formula:

$$Z_{\|}(f) = \sum_n \frac{R_{sh}(f_n)}{1 + jQ_m(f_n)\left(\frac{f}{f_n} - \frac{f_n}{f}\right)} \tag{5.38}$$

5.3.1 Comparison between the hybrid method and the mode matching technique

The shunt impedance values are compared in Tab.5.5 either for the hybrid numerical/ experimental method and for the mode matching technique.

f_{nml}^{TM}	Measured f_r $[GHz]$	Measured Q factor	Simulated R_{sh}/Q	Hybrid R_{sh}	Mode Matching R_{sh}
$0,1,0$	0.921	43265	13.2866	287421	284939
$0,1,1$	1.007	35425	54.6179	967419	1005895
$0,1,2$	1.220	38231	98.5058	1882986	1984652
$0,1,3$	1.509	42594	71.7737	1528564	1606664
$0,1,4$	1.839	46317	44.5258	1031150	1100766
$0,2,0$	2.117	66463	2.33596	77627	77929
$0,2,1$	2.164	53327	0.39714	10589	9390
$0,1,5$	2.194	54253	31.0281	841682	838327
$0,1,6$	2.557	59908	18.0553	540828	527837

Table 5.5: Comparison between hybrid and mode matching method.

The maximum difference of the shunt impedance values is less than 6% for the measurable peaks. Is also possible to see the Fig.5.12 in which are compared the hybrid method with the Lorentzian fit and mode matching.

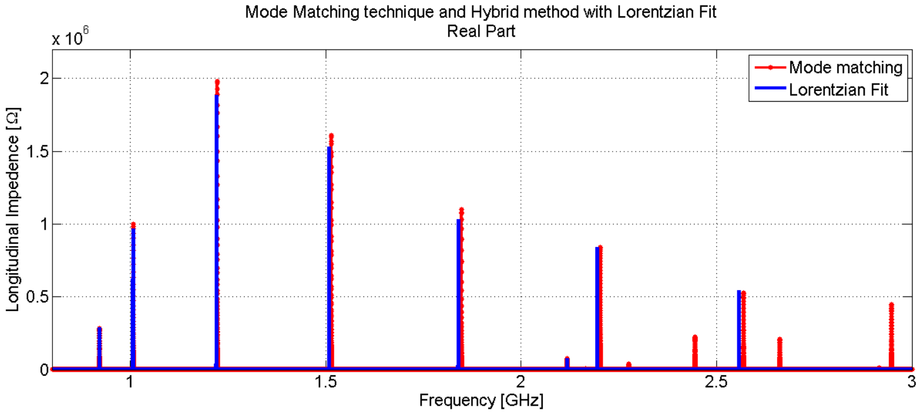

Figure 5.12: Comparison of the longitudinal real part impedance between the Mode Matching technique (blue line) and the Hybrid method with Lorentzian fit (green line).

The satisfactory results obtained by applying a numerical method on reliable experimental data in the case of the simple pillbox cavity could be the base for the future development and applications to more complex structures.

Conclusion

This thesis work has been developed within a collaboration between two groups of researches:

- from CERN of Geneva where one of the purpose of LHC experiment is to evaluate the beam coupling impedance of the goniometer, used for the beam collimation;
- from Istituto Nazionale di Fisica Nucleare (INFN) of Naples where they are developing a new experimental method to evaluate the coupling impedance in a frequency below the beam pipe cut-off frequency.

This thesis work has faced two main subjects:

- ***the global behaviour of the impedance, using the electromagnetic simulation CAD CST-Studio Suite^{TM}, in order to understand which elements of the complex goniometer geometry are more "dangerous" (see Ch.4).*** For this reason we resort to simplified structures (central chamber of the collimator) which has been made complex by adding element after element. With this method it has been possible to understand the dependence of impedance peaks in the frequency region below $1GHz$ where we expect a strong coupling interaction between the beam and the goniometer (see the Sec.4.1). In fact, these peaks are present exclusively when goniometer is in operational position, because in this case it operates as an open cavity which sees the area of motors and position sensors of the crystal.
  This part of the study has clearly shown that numerical modelling is a problematic issue for structures with non-elementary geometries which can be partially faced simplifying the devices. At the same time we need a different approach to analyze structures composed by materials with unknown or complex electromagnetic properties (e.g. the material roughness),

- ***the study and development of a new experimental/numerical method to evaluate the beam impedance in some configuration that still represent an open problem: for instance below the pipe cut-off frequency (see Ch.5).***

  For the validation of this method we used a well known structure: a pillbox cavity, which has been characterized comparing analytical formulas, numerical results and experimental measurements. As it is possible to see in Fig.5.11, reported below, the evaluations of Q-factor performed with the experimental method (telescopic setup) shows very good features of reliability. Therefore on the base of the goodness of these results we could combine them with another cavity figure of merit R_{sh}/Q described in Sec.5.3. Applying a Lorentzian fit (see the eq.5.38) it has been possible to evaluate, with a good accuracy, the coupling impedance as function of frequency (see the Fig.5.12 reported below).

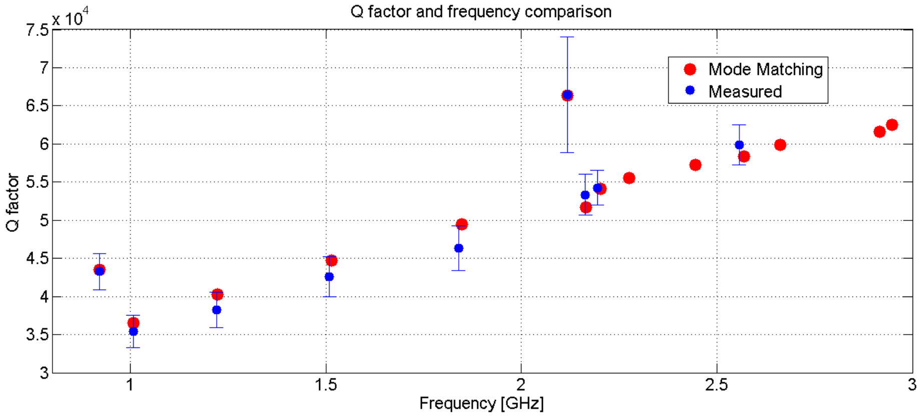

FIGURE A: Comparison between mode matching method and measurements.

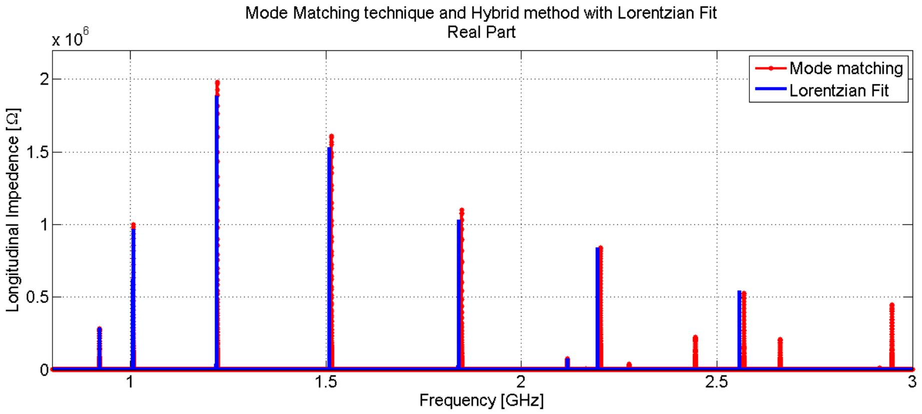

FIGURE B: Comparison of the longitudinal real part impedance between the Mode Matching technique (blue line) and the Hybrid method with Lorentzian fit (green line).

The satisfactory results obtained by applying a numerical method on reliable experimental data in the case of the simple pillbox cavity could be the base for the future development and applications to more complex structures.

Appendix A

Symmetries

The study of the UA9 goniometer has been started from simplified structure. The benefits using these structures include the possibility to use the symmetry planes, in order to decrease the number of mesh elements, the simulation time and the memory occupation and also a reliability improvement of the simulation results because is fixed a plane on which is known the electromagnetic behaviour.

To better understand the symmetry properties, has been studied a simple rectangular chamber with a top-bottom and left-right geometrical symmetry with an aspect ratio of the guide of 0.5 and a wall conductivity 10^6 S/m, and open boundaries along the z axis (Fig.A.1).

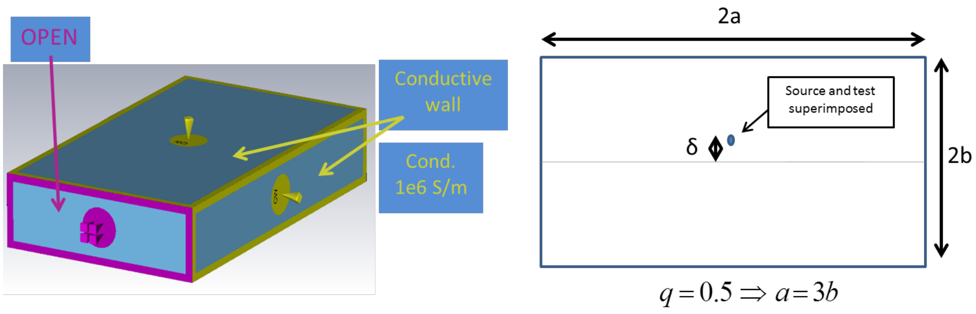

FIGURE A.1: CST rectangular pipe used for the symmetry study.

The beam and the test were displaced of a δ, that is significantly smaller than the pipe aperture, from the centre of the structure and has been evaluated the vertical generalized term of the Wake Potential.

$$W_y = W_y^{dip} y_0 + W_y^{quad} y \tag{A.1}$$

The offset of the beam δ is significantly smaller than the pipe aperture in order to neglect the non linear terms. At the first order the generalized term in a symmetric structure is composed only by the dipolar and the quadrupolar wake components (see Eq.A.1).

In the formula A.1 y_0 is the offset of the source and y is the offset of the test from the centre of the structure.

The study has been started exploiting the left-right symmetry using the YZ magnetic symmetry plane($H_z = 0$). And has been made a comparison between structure without the symmetry and the structure using the YZ magnetic plane($H_z = 0$) (see Fig.A.2).

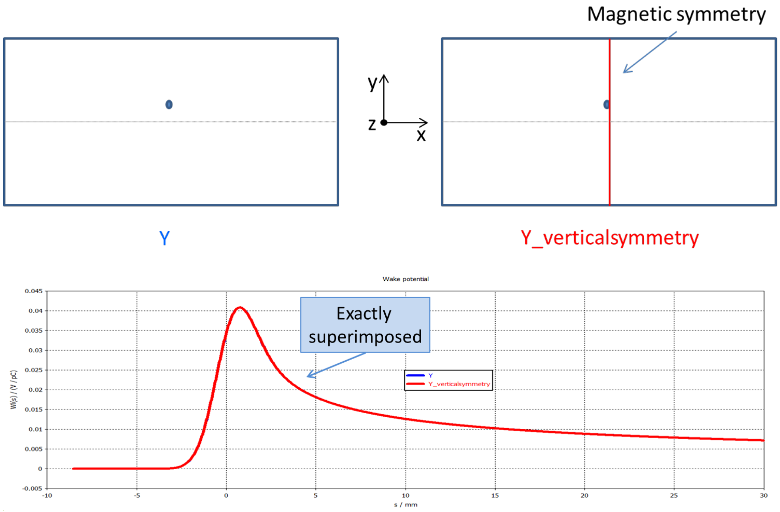

Figure A.2: Comparison between the wake potential of the structure without symmetries (blue line) and the structure with YZ magnetic symmetry (red line).

As expected the results of the wake potential in Fig.A.2 are exactly superimposed, so has been confirmed the possibility to use the magnetic symmetry plane in case of geometrical symmetry and beam on the symmetry axis. This has been possible because the beam direction is along the z axes, so the tangential component of the magnetic field in the center of the structure is zero.

To profit by all of the symmetries of the geometrical structure, so to use *1/4* symmetry, has been started to study the XZ symmetry plane.

In Fig.A.3 has been compared the structure without symmetry planes with the structure with the XZ magnetic symmetry plane($H_z = 0$).

In Fig.A.3 there is a difference between the two results. To understand the meaning of the green curve, in this case the XZ magnetic symmetry plane ($H_z = 0$) force to zero the dipolar wake so there is only the quadrupolar wake component in the formula A.1.

In the Fig.A.4 there is a comparison between the structure with the XZ magnetic symmetry plane and the standard simulation of the quadrupolar term of the wake potential.

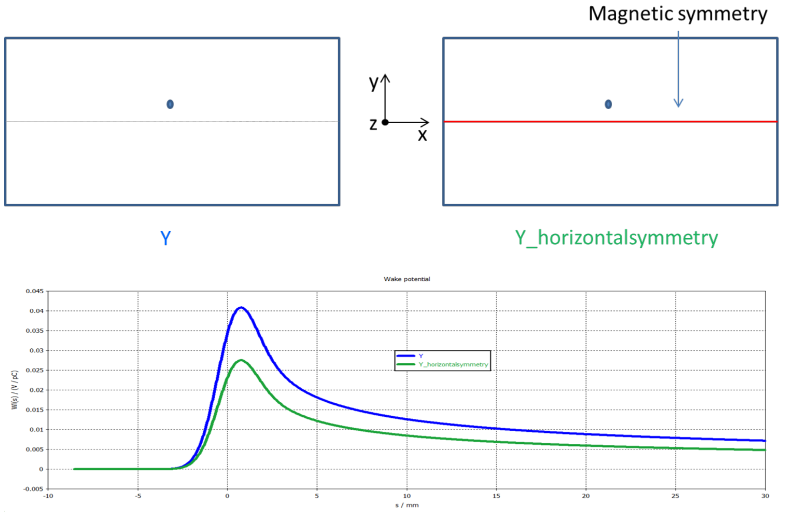

FIGURE A.3: Comparison between the wake potential of the structure without symmetries (blue line) and the structure with XZ magnetic symmetry (green line).

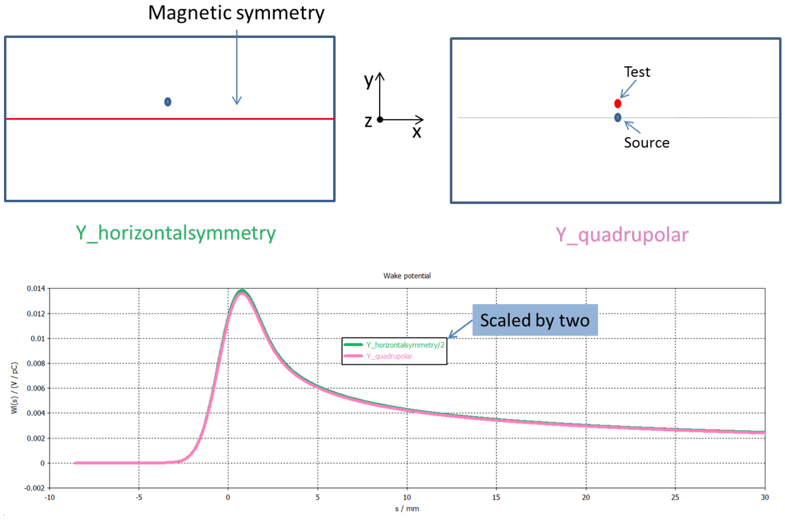

FIGURE A.4: Comparison between the wake potential of the structure with XZ magnetic symmetry divided by two (green line) and the standard simulation of the quadrupolar term of the wake potential (pink line).

Is possible to see a factor of two due to the presence of the second beam for the Image Theory.

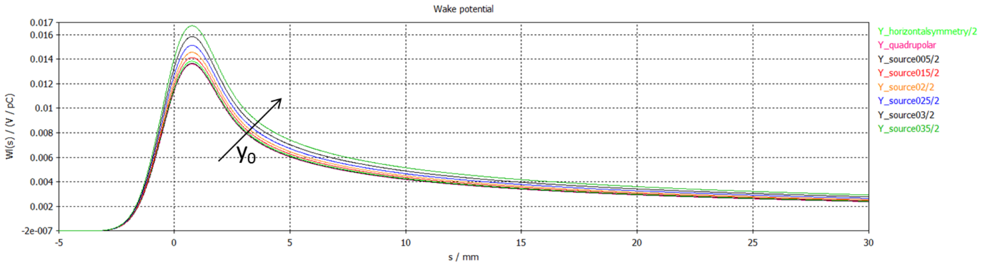

FIGURE A.5: Wake potential of the structure with XZ magnetic symmetry varying the value of the offset of the source y_0.

Therefore, the magnetic symmetry ($H_z = 0$) does not allow the dipolar term of the wake. In Fig.A.5 some simulations have been performed with different value of the offset of the source y_0. The value of the wake should not change in the approximation of the first order. But is possible to see the variation of the wake potential at different values of the offset of the beam Y_0 that is due to the higher-order terms.

$$W_y = W_y^{quad} y + k y_0^2 \tag{A.2}$$

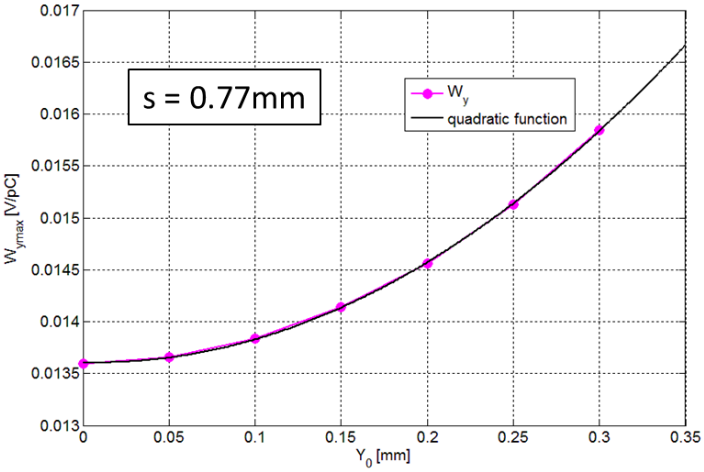

Figure A.6: Maximum values of the wake potential varying the offset of the source y_0 (violet line) and quadratic function considering *k=0.0261*.

In Fig.A.6 has been fitted the curve of the maximum values of the wake potential varying the offset of the source y_0 and is possible to see a quadratic trend considering a value of *k=0.0261*.

The same study has been performed using the XZ electric symmetry plane ($E_z = 0$). In Fig.A.7 the structure without symmetries and the structure with the XZ electric symmetry plane ($E_z = 0$) have been compared.

Dually to the magnetic case , the XZ electric symmetry plane forces to zero the quadrupolar wake so there is only the dipolar wake component.

In the Fig.A.8 there is a comparison between the structure with the XZ electric symmetry plane and the standard simulation of the dipolar term of the wake. Also in this case is possible to see a factor of two due to the presence of the second beam for the Image Theory.

The conclusion to underline is that always the quadrupolar and dipolar wake/impedance could be calculated using the same degree of geometrical symmetry of the device under test.

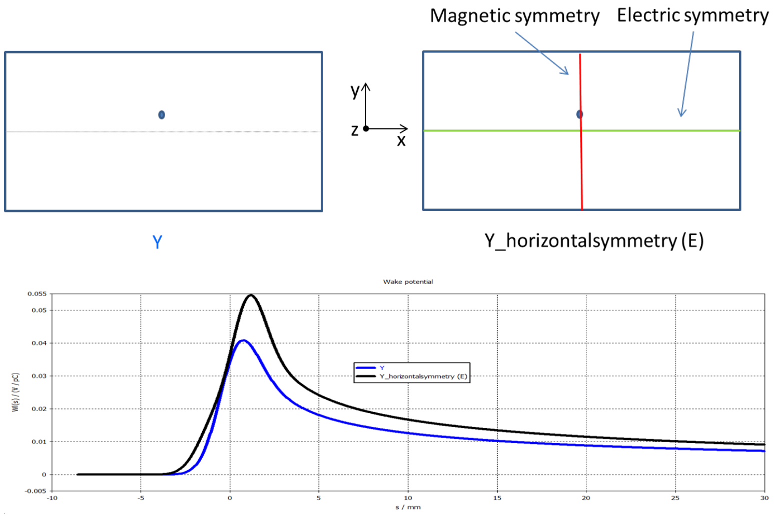

Figure A.7: Comparison between the wake potential of the structure without symmetries (blue line) and the structure with XZ electric symmetry (black line).

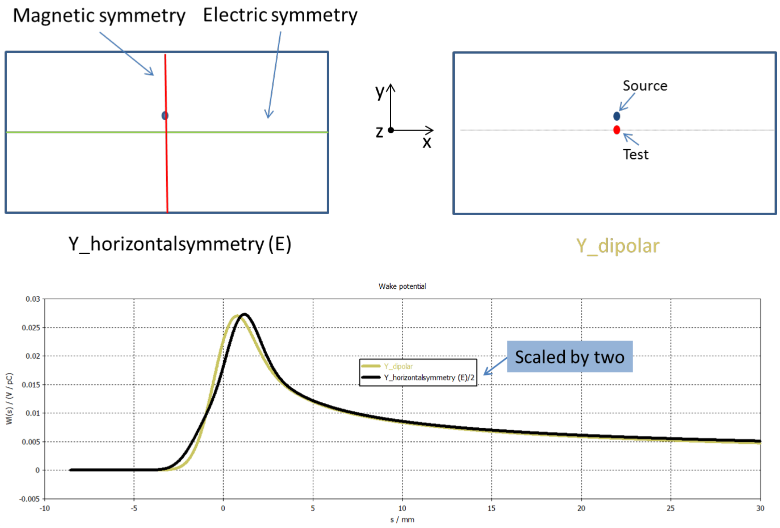

Figure A.8: Comparison between the wake potential of the structure with XZ electric symmetry divided by two (black line) and the standard simulation of the dipolar term of the wake potential (gold line).

This case has been studied for the vertical component of the wake potential, but the same study can be applied to the horizontal component rotating the axes.

Bibliography

[1] V. Kelvin Neil and Andrew M. Sessler. Longitudinal resistive instabilities of intense coasting beams in particle accelerators. *Review of Scientific Instruments*, 36(4), 1965.

[2] V G Vaccaro. Longitudinal instability of a coasting beam above transition, due to the action of lumped discontinuities. Technical Report CERN-ISR-RF-66-35. ISR-RF-66-35, CERN, Geneva, Nov 1966.

[3] L. Palumbo, Vittorio Giorgio Vaccaro, and Godehard Wustefeld. Coupling impedance in a circular particle accelerator, a particular case: Circular beam, elliptic chamber. *Nuclear Science, IEEE Transactions on*, 31(4):1011–1020, Aug 1984. ISSN 0018-9499. doi: 10.1109/TNS.1984.4333427.

[4] S A Heifets and S A Kheifets. Coupling impedance in modern accelerators. Technical Report SLAC-PUB-5297, SLAC, Stanford, CA, Sep 1990.

[5] L Palumbo, Vittorio G Vaccaro, and M Zobov. Wake fields and impedance. (physics/0309023. LNF-94-041-P):70 p, Sep 1994.

[6] Lyndon R Evans. LHC Accelerator Physics and Technology Challenges; rev. version. (LHC-Project-Report-303. CERN-LHC-Project-Report-303):6 p, Apr 1999.

[7] Carlo Zannini, Leonid Rivkin, and Giovanni Rumolo. *Electromagnetic Simulation of CERN accelerator Components and Experimental Applications*. PhD thesis, Ecole Polytechnique, Lausanne, Mar 2013. Presented 15 Apr 2013.

[8] L Palumbo and Vittorio G Vaccaro. Wake field: impedances and Green's function. 1987.

[9] Andrew M Sessler and Vittorio G Vaccaro. *Longitudinal instabilities of azimuthally uniform beams in circular vacuum chambers with walls of arbitrary electrical properties*. CERN, Geneva, 1967.

[10] Nicolas Mounet, Leonid Rivkin, and Elias Metral. *The LHC Transverse Coupled-Bunch Instability*. PhD thesis, Ecole Polytechnique, Lausanne, Mar 2012. Presented 2012.

[11] S. Heifets, A. Wagner, and B. Zotter. Generalized impedances and wakes in asymmetric structures. 1998.

[12] CST MICROWAVE STUDIO - Workflow and Solver Overview.

[13] R Losito, E Laface, and W Scandale. The UA9 Experiment at the CERN-SPS. (CERN-ATS-2009-131):3 p, Apr 2009.

[14] Walter Scandale. UA9 Report for 2013. Technical Report CERN-SPSC-2013-031. SPSC-SR-126, CERN, Geneva, Oct 2013.

[15] W. Scandale. LHC collimation with bent crystals - Agenda INFN, Sep 2011.

[16] A Danisi, C Zannini, A Passarelli, A Masi, R Losito, and B Salvant. FEM Analysis of Beam-Coupling Impedance and RF Contacts Criticality of the LHC UA9 Piezo Goniometer. (CERN-ACC-2014-0192):4 p, Jun 2014.

[17] W. Scandale. The ua9 experiment on crystal-assisted collimation at the cern-super proton synchrotron: tutorial 48. *Instrumentation Measurement Magazine, IEEE*, 17(1):28–33, February 2014. ISSN 1094-6969. doi: 10.1109/MIM.2014.6782993.

[18] L Palumbo and Vittorio G Vaccaro. Wake fields measurements. (LNF-89-035-P): 46 p, May 1989.

[19] E D.Mohl A. Faltens, C. Hartwig and A M. Sessler. An analog method for measuring the longitudinal coupling impedance of a relativistic particle beam with its environment. (8th International Conference on High Energy Accelerator), 1971.

[20] M Sands and J Rees. A Bench Measurement of the Energy Loss of a Stored Beam to a Cavity. Technical Report LBL-PEP-NOTE-95. PEP-95. SLAC-TN-2005-051, Lawrence Berkeley Nat. Lab., Berkeley, CA, Aug 1974.

[21] Vittorio G Vaccaro. Coupling impedance measurements: an improved wire method. Technical Report INFN-TC-94-023, INFN, Rome, Nov 1994.

[22] A Argan, L Palumbo, M R Masullo, and Vittorio G Vaccaro. On the Sands and Rees Measurement Method of the Longitudinal Coupling Impedance. 1999.

[23] Marco Panniello. *Numerical-analytical methods for particle accelerators*. PhD thesis, Universitá degli studi Federico II, Napoli, 2009.

[24] David M Pozar. *Microwave engineering; 4th ed.* Wiley, Hoboken, NJ, 2012.

[25] Jean G Van Bladel. *Electromagnetic Fields; 2nd ed.* Wiley, Newark, 2007.

[26] G. Franceschetti. *Campi elettromagnetici.* Bollati Boringhieri, 1983.

[27] Robert E Collin. *Field theory of guided waves; 2nd ed.* IEEE, New York, NY, 1991.

[28] Nicoló Biancacci, Luigi Palumbo, Mauro Migliorati, Elias Métral, and Benoit Salvant. *Improved techniques of impedance calculation and localization in particle accelerators.* PhD thesis, Rome, La Sapienza, Apr 2014. Presented 07 05 2014.

[29] Thomas P Wangler. *RF linear accelerators; 2nd rev. version.* Physics textbook. Wiley, Weinheim, 2008.